Authors Version - Freddi, F., Dimopoulos, C., Karavasilis, T.L. (2020) Experimental evaluation of a rocking damage-free steel column base with friction devices. Journal of Structural Engineering, 146(10): 04020217. ASCE, DOI: 10.1061/(ASCE)ST.1943-541X.0002779.

# Experimental Evaluation of a Rocking Damage-Free Steel Column Base with Friction Devices

**Fabio Freddi[1*], Christoforos A. Dimopoulos[2], and Theodore L. Karavasilis[3]**

[1] *Lecturer, Dept. of Civil, Environmental and Geomatic Engineering, University College London, London WC1E 6BT, U.K.*
[*] Corresponding Author. Tel.: +44 (0) 775 236 0204. E-mail address: f.freddi@ucl.ac.uk

[2] *Lecturer, School of Science, Engineering and Design, Teesside University, Middlesbrough, TS1 3BX, U.K.*
E-mail address: c.dimopoulos@tees.ac.uk

[3] *Associate Professor of Steel Structures, Department of Civil Engineering, University of Patras, GR-26500 Patras, Greece.*
E-mail address: karavasilis@upatras.gr

**Abstract**

The paper presents the experimental evaluation of an earthquake-resilient rocking damage-free steel column base, previously proposed and numerically investigated by the authors. The column base uses post-tensioned high-strength steel bars to control its rocking behavior and friction devices to dissipate seismic energy. It is equipped with a circular steel plate with rounded edges, which is used as a rocking base. The rounded edges prevent stress concentration and damage of the contact surfaces, while the circular shape allows rocking towards all plan directions. Contrary to conventional steel column bases, the proposed column base exhibits monotonic and cyclic moment–rotation behaviors that are easily described by analytical equations. The latter allow the definition of a step-by-step design procedure, which ensures damage-free behavior, self-centering capability and energy dissipation capacity for a target design base rotation. The experimental tests are conducted under monotonic and cyclic loads demonstrating the damage-free behavior even under large rotations. Then, the experimental results are used to validate the design procedure and to calibrate refined 3D nonlinear finite element models in ABAQUS that will allow further investigations.

KEY WORDS: Damage-free column base; Experimental test; Steel frames; Rocking; Seismic design; Structural Resilience.

## 1. INTRODUCTION

Conventional seismic-resistant structures, such as steel moment-resisting frames (MRFs) or concentrically braced frames, are designed to experience significant inelastic deformations under strong earthquakes (*e.g.,* EN1998-1-1 2005; FEMA 2000). Inelastic deformations can result in damage to the structural members and residual drifts, leading to high repair costs and disruption of the building occupation. The aforementioned socio-economic risks highlight the need for widespread implementation of minimal-damage structures, which can reduce both repair costs and downtime. Examples of such structures include self-centering moment-resisting frames (SC-MRF), systems employing structural fuses, passive energy dissipation devices, self-centering braces, among others (*e.g.,* Garlock *et al* 2007; Kim and Christopoulos 2008; Vasdravellis *et al* 2013; Dimopoulos *et al* 2016; Tzimas *et al* 2016; Dimopoulos *et al* 2019; Blomgren *et al* 2019; Symans *et al* 2008; Akcelyan *et al* 2016; Freddi *et al* 2013; Gioiella *et al* 2018). These earthquake-resilient steel frame typologies have been extensively studied during the last decade, however, further studies are needed to improve the behavior of their column bases.

Based on the capacity design philosophy of Eurocode 8 (2005) (EN 1998-1-1 2005), conventional steel column bases can be designed as full- or partial-strength joints. In the first approach, plastic hinges are developed in the bottom end of the first story columns, while in the second, the column bases are designed to dissipate energy through inelastic deformations in their main components (*i.e.,* base plates, anchor rods) (EN 1998-1-1 2005; EN 1993-1-8 2005). The design of full-strength joints leads to very strong column bases due to the over-strength factors that account for material variability (Latour and Rizzano 2013) and to conservative foundation designs because the full moment resistance of the column profile is transferred to the foundation. On the other hand, the design of partial-strength joints allows better control of the dimensions of the column bases but requires knowledge of its complex hysteretic behavior under cyclic loading, which is difficult to predict and is affected by strength and stiffness degradation (Latour and Rizzano 2013; Rodas *et al* 2016). Most importantly, for both approaches, field observations after strong earthquakes have confirmed the susceptibility of column bases to difficult-to-repair damage and residual deformations related to concrete crushing, weld fracture, anchor rod fracture, and base plate yielding (Grauvilardell *et al* 2006). In design practice, column bases are assumed to behave as a fully fixed or pinned connection and such assumption may either underestimate or overestimate the story drifts and internal member forces, thus leading to uneconomical or unconservative designs (Zareian and Kanvinde 2013; Kanvinde *et al* 2012).

A number of research efforts have proposed alternative solutions with the goal of overcoming the shortcomings of conventional column bases (*e.g.,* Kelly and Tsztoo 1977; Ikenaga *et al* 2006; Mackinven *et al* 2007; Chou and Chen 2011; Chi and Liu 2012; Yamanishi *et al* 2012; Takamatsu and Tamai 2005; Grigorian *et al* 1993; MacRae *et al* 2009; Borzouie *et al* 2015; Latour *et al* 2019; Kamperidis *et al* 2018; Wang *et al* 2019; Freddi *et al* 2017). Among the first attempts to develop minimal-damage column bases, Kelly and Tsztoo (1977), proposed and experimentally investigated a partial isolation system associated with an energy-absorbing device that could be easily replaced after an earthquake. The results of this study demonstrated the advantages of damage-free structural systems and promoted many successive studies in this direction.

Some of these research works (*e.g.,* Ikenaga *et al* 2006; Mackinven *et al* 2007; Chou and Chen 2011; Chi and Liu

2012; Yamanishi *et al* 2012; Takamatsu and Tamai 2005), have focused on the use of rocking column bases where post-tensioned (PT) bars, or yielding bolts, were used to control rocking behavior and to provide self-centering capability, while dedicated devices were used to dissipate seismic energy. Several different configurations were investigated considering different column sections, different lengths and different positions of the PT bars. Two examples of these column bases, respectively by Chi and Liu (2012) and by Yamanishi *et al* (2012), are illustrated in Fig. 1(a) and (b). While in some cases the results showed the advantages of the system in terms of improved self-centering behavior of the column base, several drawbacks were also highlighted including undesirable column axial shortening, loss of post-tensioning force and inelastic deformations. Alternatively, based on the concept of beam-to-column connections with friction devices (FDs), originally pioneered by Grigorian and Popov (1993), other authors further extended this idea to column bases. MacRae *et al* (2009) and Borzouie *et al* (2015) developed two different configurations of column base where the moment resistance and the energy dissipation were provided by friction resistance activated by the relative movement of the column flanges with respect to foundation flange plates with slotted holes. These configurations, respectively illustrated in Fig. 1(c) and (d), allowed to achieve superior behavior under loading in the column strong-axis direction, while damage and stiffness degradation was observed under loading of the column in the weak-axis direction.

Recently, Latour *et al* (2019) developed a self-centering base plate connection where FDs were coupled with pre-loaded threaded bars and disk springs as illustrated in Fig. 1(e). The experimental results demonstrated that the system was able to provide energy dissipation and self-centering capabilities along with damage-free behavior. In addition, Kamperidis *et al* (2018) and Wang *et al* (2019), studied two types of low-damage self-centering steel column base connections illustrated respectively in Fig. 1(f) and (g). In both cases, the column base was composed by a concrete-filled square steel section and used external PT strands to control rocking behavior. Two different types of yielding devices, respectively hourglass shape steel yielding devices and sandwiched energy dissipaters, were used to dissipate the seismic energy. Both the numerical simulations and the experimental results demonstrated self-centering behavior and stable energy dissipation of both column base connections demonstrating low residual drifts. However, all the configurations investigated and described so far, do not prevent high stress concentration and damage at the onset of rocking. In addition, they do not provide solutions to control the response of the column base in different plan directions except from the principal direction of the column cross-section.

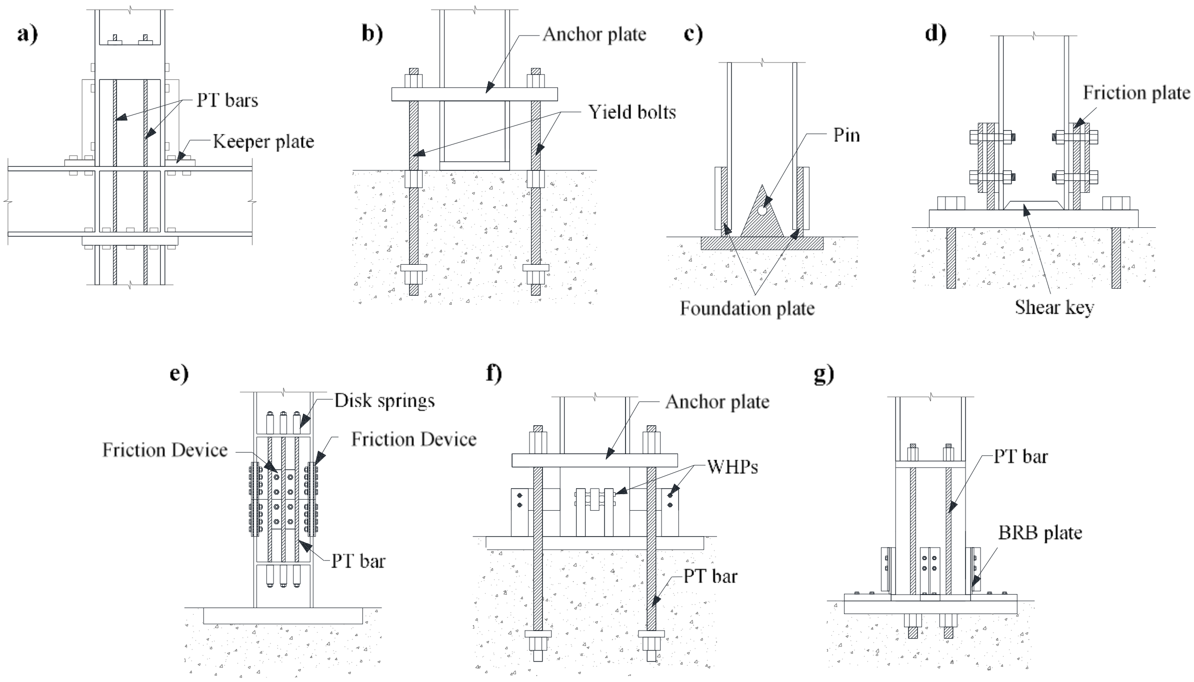


**Fig. 1.** Novel CBs proposed by: (a) Chi and Liu (2012); (b) Yamanishi *et al* (2012); (c) MacRae *et al* (2009); (d) Borzouie *et al* (2015); (e) Latour *et al* (2019); (f) Kamperidis *et al* (2018); (g) Wang *et al* (2019).

In 2017, Freddi *et al* (2017) proposed and numerically investigated a rocking damage-free steel column base, that can be employed to reduce residual deformations and damage in 'innovative' MRFs. The proposed column base, similarly to previous studies, used PT high-strength steel bars to control the rocking behavior while FDs were used to dissipate the seismic energy. Amongst others, the main advances with respect to other studies, relates to the circular steel plate with rounded edges which is used as rocking base. The rounded edges prevent stress concentration and damage of the contact surfaces while rocking, while the circular shape allows rocking in all plan directions. Freddi *et al* (2017) provided simple analytical equations to describe both the monotonic and cyclic moment–rotation behavior considering also the possible limit states. These allowed the definition of a design procedure based on non-dimensional parameters and a simple graphical tool. Both the analytical moment–rotation equations and the design procedure were validated with the aid of 3D nonlinear finite element (FE) simulations in ABAQUS (2013) that allowed also to evaluate the local behavior of the components. On the other side, a simplified 2D model of the rocking column base was also developed in OpenSees (2006) (McKenna *et al* 2006) to assess the influence of the proposed column base on the global behavior of a structural system. The OpenSees model was used to conduct nonlinear dynamic analyses on a five-story, five-bay by three-bay steel SC-MRFs with the conventional and proposed rocking column base. The results showed that the proposed rocking column base can fully protect the first story columns from yielding and eliminates the first story residual drift without detrimental effects on peak inter-story drifts.

The present paper experimentally evaluates a 3/5 scaled specimen of the rocking damage-free steel column base proposed in Freddi *et al* (2017) under monotonic and cyclic quasi-static loads. The experimental campaign included tests for the characterization of the FDs, required for the definition of important parameters, such as the friction coefficient of the sliding materials and coupon tests for the characterization of the materials. The experimental results demonstrated the damage-free behavior of the column base up to the target design rotation and the ability to limit damage only to few easily replaceable components even under large rotations. The experimental results were also compared and used to calibrate FE models in ABAQUS that will allow further numerical investigations.

## 2. ROCKING DAMAGE-FREE STEEL COLUMN BASE

### *2.1 Structural details*

Fig. 2 shows the column base proposed and numerically evaluated by Freddi *et al* (2017). A thick steel plate with rounded edges is welded to the bottom of a circular hollow steel section. The rounded edges help the column base to avoid stress concentrations and damage while rocking. Four PT high strength steel bars (or alternatively strands) are symmetrically placed around the center of the column base to increase the axial force in the column and further control the rocking behavior. The PT bars are anchored to the bottom of the foundation (by running them through steel ducts) and to a thick plate welded on the top of the hollow steel section (see the anchor plate in Fig. 2(a)). FDs are placed on the four sides of the column base to provide energy dissipation during rocking. As shown in Fig. 3(a), the FDs consist of two external steel plates bolted to the base plate, an internal steel plate welded to the circular hollow section, and two plates of brass material glued to the external plates at the interface between the external and internal plates. Rocking of the column base results in sliding of the internal plate with respect to the brass and external plates, and thus, dissipates energy through friction. The internal plate is drilled with inclined slotted holes to enable sliding, while the external plates and the brass plates are drilled with aligned rounded holes to accommodate pre-tensioned bolts that are used to tune the friction force in the FDs. The dimensions of the inclined slotted holes are chosen to accommodate the superposition of all possible bolt travel paths during rocking, as shown in Fig. 3(a) (Wolski *et al* 2009). Shear resistance is provided by friction between the base plate and the circular steel section, while as shown in Fig. 3(b), a shear key is included to prevent sliding in case the shear force overcomes the friction resistance. The shear key is designed, such that in the absence of slippage, there is no contact between its coupling parts during rocking.

*2.2 Moment-rotation behavior*

Fig. 4(a) shows the dimensions of the column base that control the moment-rotation behavior in the rocking direction, *i.e.*, $b$ is the dimension of the contact surface; $b_{PT}$ is the distance among the PT bars; $b_{FD}$ is the distance among the centers of the FDs and $h_{FD}$ is the distance of the centers of the FDs from the base plate. Fig. 4(b) shows the column base at the onset of rocking with respect to its right edge under the effect of the internal axial force ($N$), shear force ($V$), and bending moment ($M$). In Fig. 4(b), $F_{PT,u}$ and $F_{PT,d}$ are the forces in the PT bars, while $F_{FD,u}$, $F_{FD,d}$ and $F_{FD,c}$ are the forces in the FDs. The subscripts $u$ and $d$ denote whether the point of application of these forces will move upwards or downwards during rocking. The subscript $c$ denotes the force in each of the two central FDs. The lever arms of the forces with respect to the center of rotation $z_{PT,u}$, $z_{PT,d}$, $z_{FD,u}$, $z_{FD,c}$, $z_{FD,d}$ are easily derived from the main dimensional parameters as discussed in Freddi *et al* (2017).

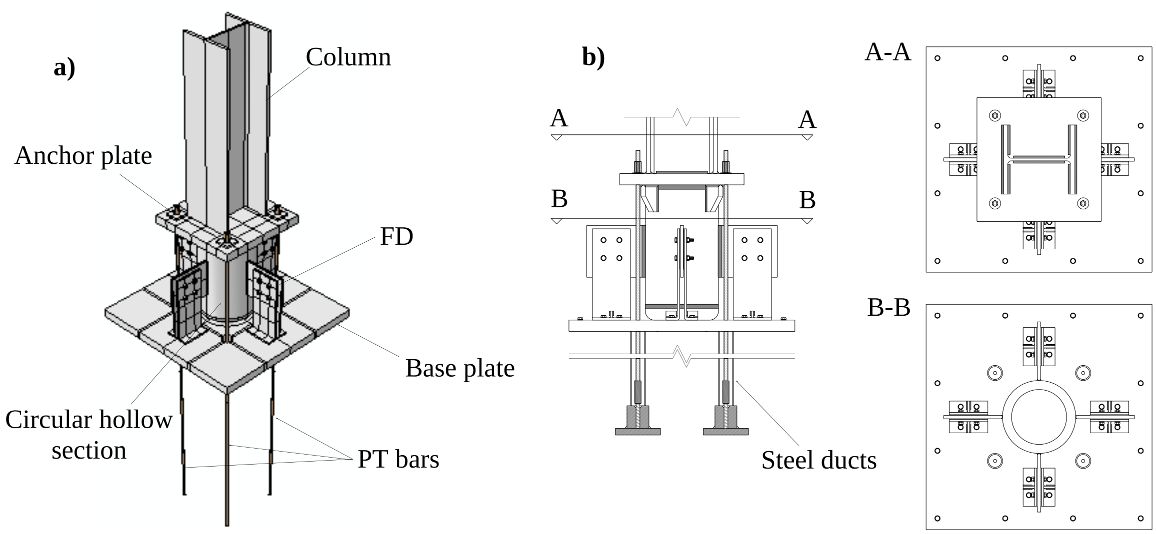


**Fig. 2.** Column base (a) 3D view and (b) lateral view and sections

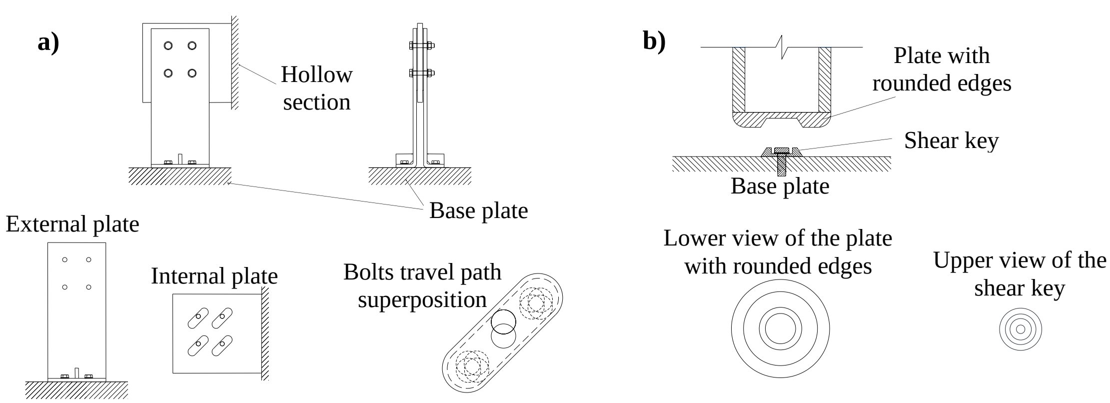


**Fig. 3.** (a) Details of the friction device (FD) and (b) steel plate with rounded edges and shear key

The moment contribution of the axial force, $N$, is given by

$$M_{\mathrm{N}} = N \cdot \frac{b}{2} \tag{1}$$

The forces in each PT bar are function of the rotation, $\theta$, of the column base and are given by

$$F_{\mathrm{PT,u}} = T_{\mathrm{PT}} + K_{\mathrm{PT}} \cdot z_{\mathrm{PT,u}} \cdot \theta \qquad for \quad \theta \leq \theta_{\mathrm{PT,u,y}} \tag{2.a}$$

$$F_{\mathrm{PT,d}} = T_{\mathrm{PT}} - K_{\mathrm{PT}} \cdot z_{\mathrm{PT,d}} \cdot \theta \qquad for \quad \theta \leq \theta_{\mathrm{PT,d,f}} \tag{2.b}$$

where $T_{\mathrm{PT}}$ is the initial post-tensioning force of each PT bar; $K_{\mathrm{PT}} = E_{\mathrm{PT}}A_{\mathrm{PT}}/L_{\mathrm{PT}}$ is the stiffness of each PT bar; $E_{\mathrm{PT}}$, $A_{\mathrm{PT}}$ and $L_{\mathrm{PT}}$ are respectively the Young's modulus, the cross-sectional area, and the length of each PT bar; $\theta_{\mathrm{PT,u,y}}$ is the rotation at which the PT bars (in position $u$) yield; and $\theta_{\mathrm{PT,d,f}}$ is the rotation at which the force of the PT bars (in position $d$) becomes zero, *i.e.*, when loss of post-tensioning occurs. The PT bars should be designed to avoid either yielding or loss of post-tensioning for a target rotation $\theta_{\mathrm{T}}$. The moment contribution of the PT bars is given by

$$M_{\mathrm{PT}}(\theta) = 2\left[T_{\mathrm{PT}}\left(z_{\mathrm{PT,u}} - z_{\mathrm{PT,d}}\right) + K_{\mathrm{PT}}\left(z_{\mathrm{PT,u}}^2 + z_{\mathrm{PT,d}}^2\right)\theta\right] \qquad for \;\; \theta \leq \theta_{\mathrm{T}} \tag{3}$$

The friction force, $F_{\mathrm{FD,i}}$, for each friction surface is given by

$$F_{\mathrm{FD,i}} = \mu_{\mathrm{FD}} \cdot n_{\mathrm{b}} \cdot N_{\mathrm{b}} \quad \text{with } \mathrm{i} = u, c, d \tag{4}$$

where $\mu_{\mathrm{FD}}$ is the friction coefficient of the surfaces in contact; $n_{\mathrm{b}}$ is the number of bolts and $N_{\mathrm{b}}$ is the bolt pre-loading force. The moment contribution of the FDs is given by

$$M_{\mathrm{FD}} = n_{\mathrm{FD}} \cdot F_{\mathrm{FD}}\left(z_{\mathrm{FD,u}} + 2 \cdot z_{\mathrm{FD,c}} + z_{\mathrm{FD,d}}\right) \tag{5}$$

Fig. 5(a) shows the moment contributions of the axial force, $M_{\mathrm{N}}$; of the PT bars, $M_{\mathrm{PT}}$; and of the FDs, $M_{\mathrm{FD}}$. The decompression moment, $M_{\mathrm{E}}$, and the moment at the onset of rocking, $M_{\mathrm{D}}$, are given by

$$M_{\mathrm{E}} = M_{\mathrm{N}} + M_{\mathrm{PT,0}} \qquad M_{\mathrm{D}} = M_{\mathrm{E}} + M_{\mathrm{FD}} \tag{6}$$

where $M_{\mathrm{PT,0}}$ is the moment provided by the PT bars at zero rotation, *i.e.*, $\theta = 0.0$ in Eq. (3).

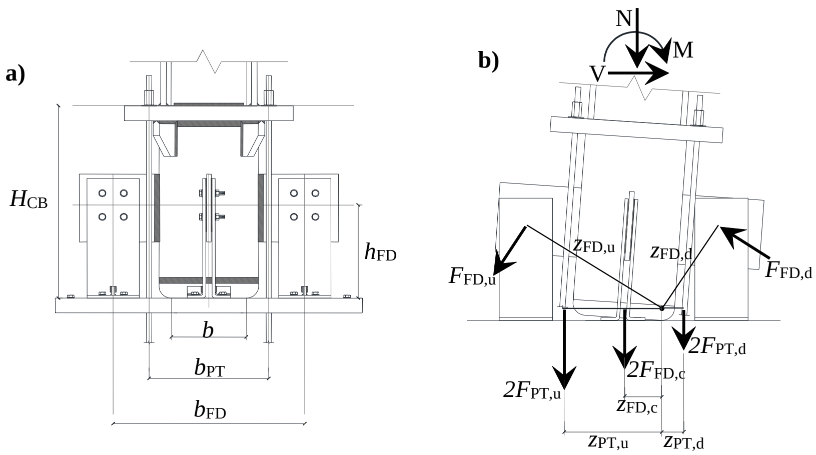


**Fig. 4.** Column base (a) fundamental dimensions; (b) forces and lever arms of the friction devices (FDs) and post-tensioned (PT) bars during rocking for loading from left to right

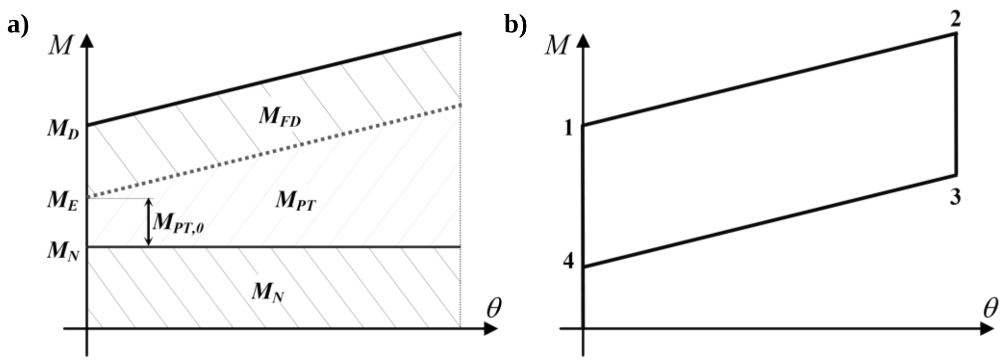


**Fig. 5.** Moment-rotation behavior of the column base. (a) Moment contribution of the axial force, $M_{\mathrm{N}}$; of the post-tensioned (PT) bars, $M_{\mathrm{PT}}$; and of the friction devices (FDs), $M_{\mathrm{FD}}$ and (b) hysteretic behavior

The rotational stiffness contribution of the PT bars and the moments corresponding to points 1 to 4 of the cyclic moment-rotation behavior of the column base in Fig. 5(b) are given by

$$S_{\mathrm{PT}} = 2K_{\mathrm{PT}}\left(z_{\mathrm{PT,u}}^2 + z_{\mathrm{PT,d}}^2\right) \tag{7}$$

$$M_1 = M_{\mathrm{D}} = M_{\mathrm{N}} + M_{\mathrm{PT,0}} + M_{\mathrm{FD}} \tag{8.a}$$

$$M_2 = M_{\mathrm{D}} + S_{\mathrm{PT}}\theta_2 \tag{8.b}$$

$$M_3 = M_{\mathrm{D}} + S_{\mathrm{PT}}\theta_2 - 2M_{\mathrm{FD}} \tag{8.c}$$

$$M_4 = M_{\mathrm{D}} - 2M_{\mathrm{FD}} \tag{8.d}$$

To ensure that the column base provides full self-centering capability, the following relation should be satisfied

$$M_4 \geq 0 \qquad M_E \geq M_{FD} \tag{9}$$

## 3. SPECIMEN DESIGN

A column extracted from a building frame was used as case study for the experimental tests. The minimum and maximum axial forces, $N_{Ed}$, from the seismic load combination were equal to 510.3 kN and 565.3 kN, respectively. The axial force from the gravity load of the seismic load combination, $N_{Ed,G}$, was equal to 537.8 kN and was employed for the design, while the minimum and maximum forces were successively used to assess its adequacy. The cross-section of the column is a HEB 300.

The experimental test was conducted on a 3/5 scaled model (*i.e.*, scaling factor $\lambda = 0.6$) of the prototype column base. The specimen of the column base was designed based on the dimensions of the scaled column. The scaling factor $\lambda = 0.6$ was chosen based on the capabilities of the lab and the model scaling was made assuming material scaling identity. Length units were scaled by $\lambda$ while areas and forces were scaled by $\lambda^2$. Table 1 contains a comprehensive list of the similitude scaling factors between the prototype and the test frames.

**Table 1**. Similitude scaling factors

| Scaling quantity | Units | Dimensional scale requirement | Required scale factor |
|---|---|---|---|
| Stress | S | 1 | 1 |
| Length or Displacement | L | $\lambda$ | 0.6 |
| Area | $L^2$ | $\lambda^2$ | 0.36 |
| Section Moduli | $L^3$ | $\lambda^3$ | 0.216 |
| Moment of Inertia | $L^4$ | $\lambda^4$ | 0.1296 |
| Force | $F=S\times L^2$ | $\lambda^2$ | 0.36 |
| Moment | $F\times L=S\times L^3$ | $\lambda^3$ | 0.216 |

The column used in the experimental test was a UC 203×203×46, which has similar dimensions with the prototype column base HEB 300 scaled by $\lambda$. The maximum $N_{Ed}$ and $N_{Ed,G}$ scaled by $\lambda^2$ are equal to 203.5 kN and 193.6 kN, respectively. The bending moment resistance $M_{N,Rd}$ evaluated according to the Eurocode 3 (2005) (EN 1993-1-1 2005) is not influenced by the axial force up to a value $N_{Ed}$ equal to 247 kN, and hence, for the considered case, the bending moment resistances in the two directions are $M_{N,Rd,y}$ = 176.58 kNm and $M_{N,Rd,z}$ = 81.97 kNm, respectively. The target rotation was assumed equal to $\theta_T$ = 0.03 rad.

Based on the geometry of the column cross-section, the fundamental dimensions of the column base (*i.e.*, $b$, $b_{PT}$, $b_{FD}$, and $h_{FD}$) were selected. A circular hollow section with a 193.7 mm diameter and 30 mm thickness was adopted. A circular steel plate with the same diameter was welded at the bottom of the hollow section. Standard mechanical processing provided this plate with rounded circular edges having a radius of 30 mm as well as with appropriate space to accommodate the shear key. The contact surface had a dimension $b$ equal to 143 mm. Due to low availability of PT bars with small dimensions, 7 wire strands complying with the requirements of the BS 5896: 2012 (2012), were used in the experiment. The anchor plate of the post-tensioned strands in the top of the hollow steel section was rectangular and had width, length, and thickness equal to 330 mm, 415 mm and 50 mm, respectively, while the distance between the strands $b_{PT}$ was equal to 255 mm. The material properties assumed for the design, which are reported in Table 2 ($f_y$: yield stress; $f_u$: ultimate stress; $E$: Young's modulus; $\beta$: strain hardening ratio and $\nu$: Poisson's coefficient), were selected on the basis of experimental results (Coelho *et al* 2004; Haremza *et al* 2013) and on test certificates provided by the suppliers.

**Table 2**. Material properties assumed for the design

| Elements | | $f_y$ [ MPa ] | $f_u$ [ MPa ] | $E$ [ GPa ] | $\beta$ | $\nu$ |
|---|---|---|---|---|---|---|
| Column and plates | S 355 JR | 355 | 510 | 210 | 0.00338 | 0.30 |
| Post-tensioned strands | BS 5896:2012 | 1885 | 1995 | 195 | 0.01193 | 0.30 |
| Bolts | Class 10.9 | 900 | 1000 | 210 | 0.00855 | 0.30 |
| Brass | C46400 half hard | 200 | 450 | 100 | 0.00839 | 0.35 |

The design was performed according to the methodology proposed by Freddi *et al* (2017), which is based on the following Eqs.

$$\kappa = \frac{1}{2A_{PT} f_{y,PT}\left(z_{PT,u} - z_{PT,d}\right)}\left[\frac{M_T - 2\frac{E_{PT}A_{PT}}{L_{PT}}\left(z_{PT,u}^2 + z_{PT,d}^2\right)\theta_T}{1+\frac{1}{\alpha_{sc}}} - N_{Ed,G}\frac{b}{2}\right] \tag{10}$$

$$\kappa \le 1 - \frac{E_{PT}\cdot z_{PT,u}\cdot\theta_T}{f_{y,PT}\cdot L_{PT}} = \kappa_{max} \tag{11}$$

$$\kappa \ge \frac{E_{PT}\cdot z_{PT,d}\cdot\theta_T}{f_{y,PT}\cdot L_{PT}} = \kappa_{min} \tag{12}$$

where $M_T = M_{N,Rd}/\gamma_T$ is the moment at the target rotation that through the safety coefficient $\gamma_T$ protects the column from yielding, while $\alpha_{sc} = M_E/M_{FD}$ is a design parameter that control the self-centering capabilities of the column. $A_{PT}$, $L_{PT}$ and $\kappa$ are the design variables of the problem and are respectively the area, the length, and the stress ratio of the post-tensioned strands (*i.e.*, $\kappa = \sigma_{PT}/f_{y,PT}$ where $\sigma_{PT}$ and $f_{y,PT}$ are respectively the stress and the yield stress of the strands) that allows definition of the value of the initial post-tensioning force. Once the area of the PT strands, $A_{PT}$, is selected, Eq. (10) is used to define the initial stress ratio of the post-tensioning strands, $\kappa$, as well as their length, $L_{PT}$, in order to meet the design requirements, *i.e.*, to limit the maximum moment at the design rotation $\theta_T$ and to provide self-centering capability. At the same time, Eqs. (11) and (12) constrain the range of values for $\kappa$ and $L_{PT}$ such that the limit states defined for the strands, *i.e.*, yielding (corresponding to $\kappa_{max}$) and loss of post-tensioning force (corresponding to $\kappa_{min}$) in the strands, are reached for rotations equal, or higher, than the design rotations $\theta_T$. More details on the design procedure are provided by Freddi *et al* (2017).

Considering 7 wire strands of 9.3 mm with an equivalent area of $A_{PT}$ = 52 mm$^2$, Fig. 6(a) shows the variation of $\kappa$ with respect to $L_{PT}$. The coefficients $\gamma_T$ and $\alpha_{sc}$ were assumed equal to 1.165 and 1.10, respectively. Any pair of $\kappa$ and $L_{PT}$ with values within the highlighted 'acceptable zone' can be selected. However, the optimum design is the one that satisfies the design criteria and minimizes the length of the PT bars, and hence, is the one that is graphically identified by the 'Design point' in Fig. 6(a). The design procedure provided an $L_{PT}$ equal to 805 mm and $\kappa$ equal to 0.2175. The latter corresponds to a $T_{PT}$ equal to 21.3 kN. In this case, the rotations $\theta_{PT,u,y}$ and $\theta_{PT,d,f}$ are equal to 0.0306 rad and 0.0302 rad, respectively. Fig. 6(b) shows the moment-rotation behavior for the column base gap opening mechanism. The decompression moment, $M_E$, the moment at the onset of rocking, $M_D$, and the moment provided by the FDs, $M_{FD}$, are equal to 19.94 kNm, 38.07 kNm and 18.13 kNm, respectively. Fig. 6(b) shows also the bending moment resistance of the upper column, $M_{N,Rd}$, which is higher than the moment of the column base connection corresponding to the design rotation $\theta_T$.

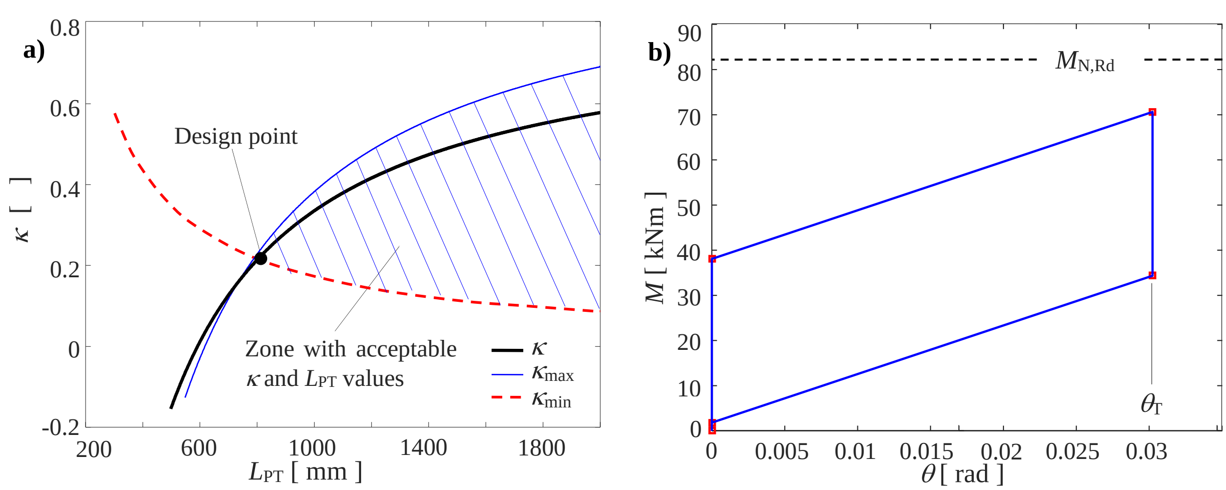


**Fig. 6.** (a) Variation of $\kappa$ with respect to $L_{PT}$ for $A_{PT}$ = 52 mm$^2$ and (b) moment-rotation behavior of the column base

Once the strands were designed, $M_{FD}$ was derived by $M_E$ and $\alpha_{sc}$ and then the FDs could be designed by selecting appropriate values of the parameters in Eq.s (4) and (5). FDs were introduced on the four sides of the column base, and the relevant dimensions were $b_{FD}$ = 465 mm and $h_{FD}$ = 250 mm. Hence, the required friction force in each friction surface of the four FDs obtained by Eq. (5) was $F_{FD}$ = 10.87 kN. The thickness of the internal and external plates of the FDs were 10 mm and 8 mm, respectively. Two 3 mm thick brass plates were used as friction interfaces, and two M12 class 10.9 bolts were used to apply the pre-loading force by tightening. The friction coefficient at the brass-steel interface was evaluated by preliminary tests described in Section 5. Successively, the pre-loading force was defined based on the friction coefficient to achieve the required friction force. The dimensions of the slotted holes were designed to allow a rotation larger than the target rotation $\theta_T$ without bearing of the bolts on the plates (*i.e.*, about 0.06 rad). Fig. 7 summarizes the geometry of the column base.

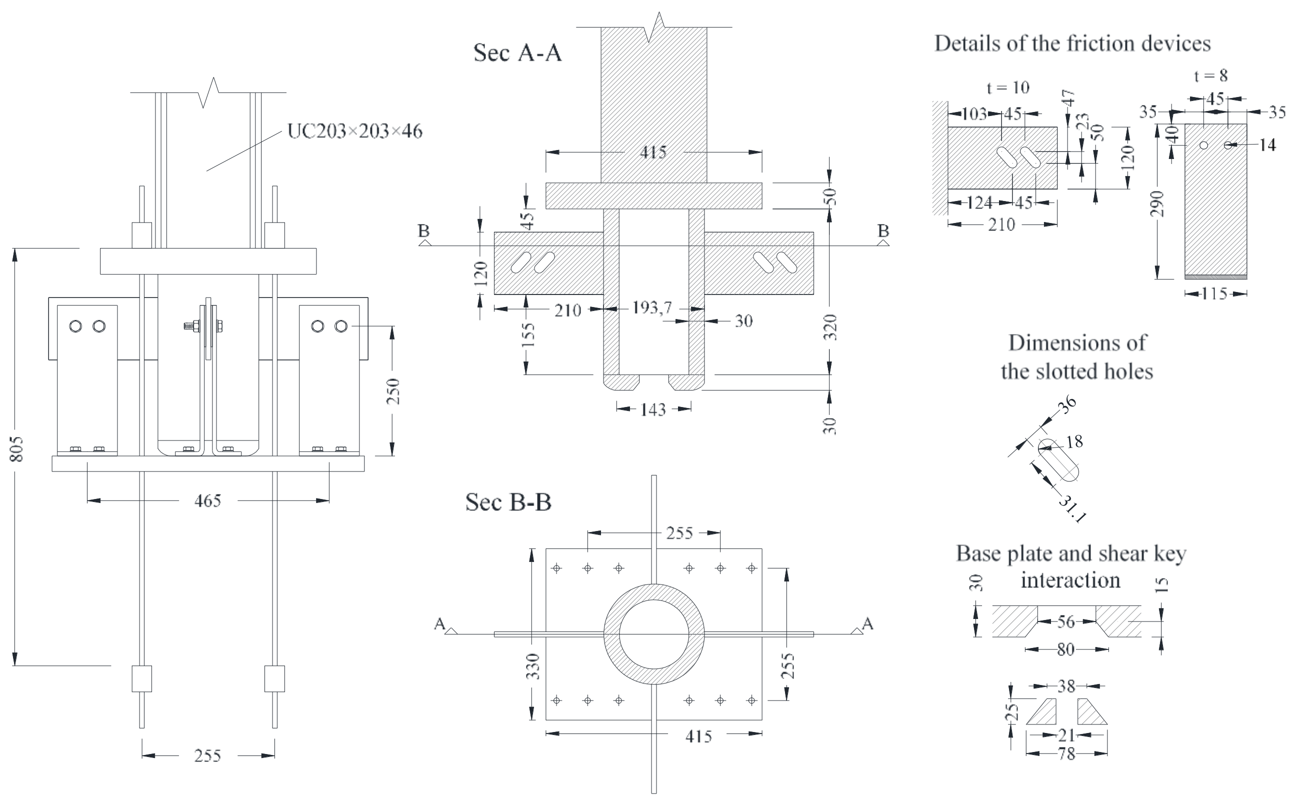


**Fig. 7.** Geometry of the specimen (dimensions in mm)

## 4. INSTRUMENTATION

Amongst others, hydraulic jacks, load cells, linear variable differential transformer (LVDT), strain gauges and a torque wrench have been used during the tests. Specifications of the hydraulic jacks and load cells are listed in Table 3 and Table 4. 10 mm linear strain gauges with mild steel compensation have been employed, while the Norbar PRO 100 1/2" torque wrench with a min and max torque of 20 and 100 Nm has been used to control the tightening of the bolts. In addition, the universal testing machine DARTEC 9500 have been used for the characterization tests of the FDs and for the coupon tests of the steel materials. Data acquisition and tests management have been performed in LabView.

**Table 3**. Hydraulic jacks employed in the tests

| Actuators | Acronym | Use | Max force [ kN ] | Stroke [ mm ] | Weight [ kg ] |
|---|---|---|---|---|---|
| Servocon System | | Application of the horizontal force | ±250 | ±150 | |
| Hi-Force HHS102 | HJA | Post-tensioning of strands | +110 | +50 | 3 |
| Yale YCS 57-70 | HJB | Post-tensioning of PT bars | +567 | +70 | 25 |

**Table 4**. Load cells employed in the tests

| Load Cells | Acronym | Measuring | Max force [ kN ] |
|---|---|---|---|
| Novatech F207 | LCA | Axial force in the bolts of the FDs | +80 |
| Novatech F313 | LCB | Axial force in the 7 wire strands (9.3 mm) | +200 |
| Novatech F203 | LCC | Axial force in the PT bars (15 mm) | +600 |

## 5. CHARACTERIZATION OF THE FRICTION DEVICES

The friction force, $F_{\mathrm{FD,i}}$, of each friction surface is given by Eq. (4) and is affected by the bolts pre-loading force, $N_{\mathrm{b}}$, and the friction coefficient of the brass-steel interface, $\mu_{FD}$. The preliminary tests described in this section allowed to characterize the FDs parameters to gain confidence in: *i)* the definition of the bolts pre-loading force, $N_{\mathrm{b}}$, used in the tests and *ii)* the definition of the friction coefficient, $\mu_{\mathrm{FD}}$, for the interface materials.

### *5.1 Relationship between torque and the bolt pre-loading force*

The bolts pre-loading force can be determined from the tightening torque by the following equation

$$N_{\mathrm{b}} = \frac{T_{\mathrm{b}}}{\alpha \cdot d} \tag{13}$$

where $T_{\mathrm{b}}$ is the value of the tightening torque, $d$ is the bolt diameter, and the recommended value of $\alpha$ is equal to 0.2 (Latour *et al* 2015). It was observed by previous studies that this relationship may under- or over-estimate the bolt pre-loading force, $N_{\mathrm{b}}$, by 20% due to different bolt type and differences in temperature, humidity, thread conditions, lubrication, etc. Hence, the characterization tests aimed at deriving the $\alpha$ parameter that best described the relationship between the tightening torque $T_{\mathrm{b}}$ and bolt pre-loading force, $N_{\mathrm{b}}$, for the M12 bolts Class 10.9 used in the tests.

Characterization tests were performed considering 30 bolts with 9 different torque values from 20 Nm to 100 Nm. The tightening torques were applied by a Norbar torque wrench, while the bolt's pre-loading force was measured with load cells (LCA in Table 4). Fig. 8(a) shows the test setup, while Fig. 8(b) shows the experimental results. Regression of a total of 270 samples provided a value for $\alpha$ equal to 0.1743.

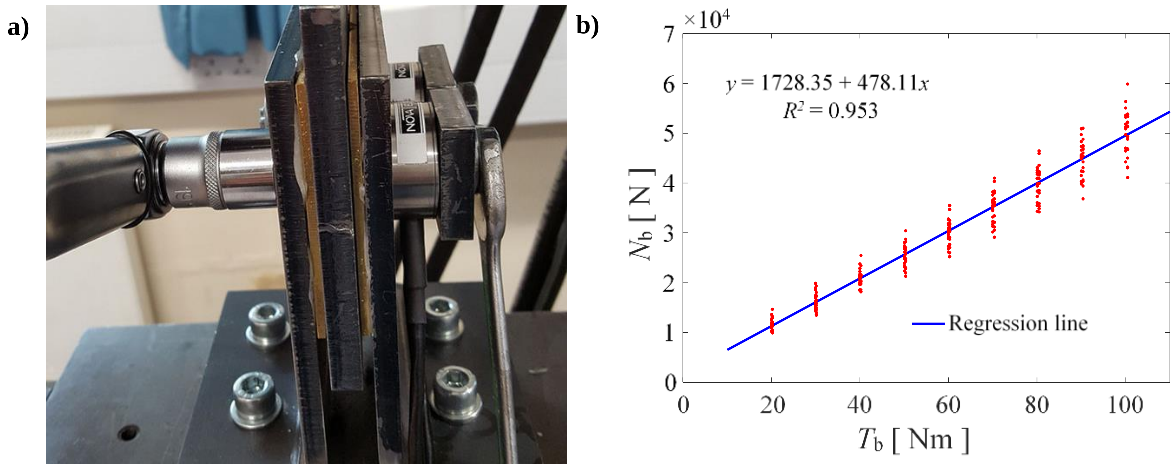


**Fig. 8.** Characterization test for the friction devices (FDs). Relationship between the tightening torque $T_b$ and the bolt pre-loading force $N_b$. (a) Representation of the tests' setup; (b) test results and interpolation curve

### *5.2 Tests for the friction coefficient of the materials interface*

This part of the study provided the static and kinetic friction coefficient of the brass-steel interface, $\mu_{FD}$, allowing also the evaluation of its variability during the cyclic displacement histories. To allow for relative displacements between the plates in the friction surfaces and to accommodate the travel path of the bolts, the inner plate of the FD, had slotted holes with dimensions of 44 by 15 mm as shown in Fig. 9(a). The two outer steel plates and the inner brass friction plates in Fig. 9(b) and (c) had circular holes and were glued together with Araldite Epoxy Adhesive. The clamping force was applied by two M12 bolts 10.9 class and the holes were of 14 mm, leaving extra tolerance with respect to the recommendations of the Eurocode 3 (EN 1993-1-8 2005). The dimensions of the friction surfaces were the same as for the FDs used in the tests of the column base. The brass material was 'C46400 half hard', while the material used for the steel components was S355.

Quasi-static tests were performed using the configuration showed in Fig. 10 and were carried out under 20 loading cycles with a linear variation of the displacement, a constant amplitude of ±10 mm, and a frequency equal to 0.25 Hz as shown in Fig. 12. Fig. 11(a) shows two instants during the test that correspond to the maximum and minimum displacements, while Fig. 11(b) and (c) show, respectively, the internal plate with slotted holes and one brass plate after the test. Four tests were conducted for different levels of pre-loading force, *i.e.*, starting from 10 kN up to 25 kN, with an increment of 5 kN at each step. The initial pre-loading force in the bolts, $N_b$, and its variation during the tests was monitored with load cells (LCA in Table 4).

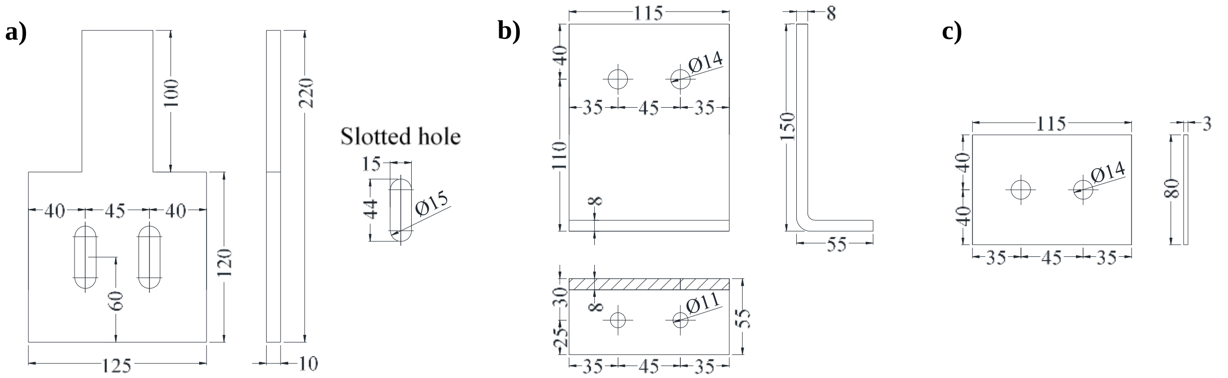


**Fig. 9.** Characterization test for the friction devices (FDs). Friction coefficient. (a) Internal plate with slotted holes; (b) external plate and (c) brass plate (dimensions in mm)

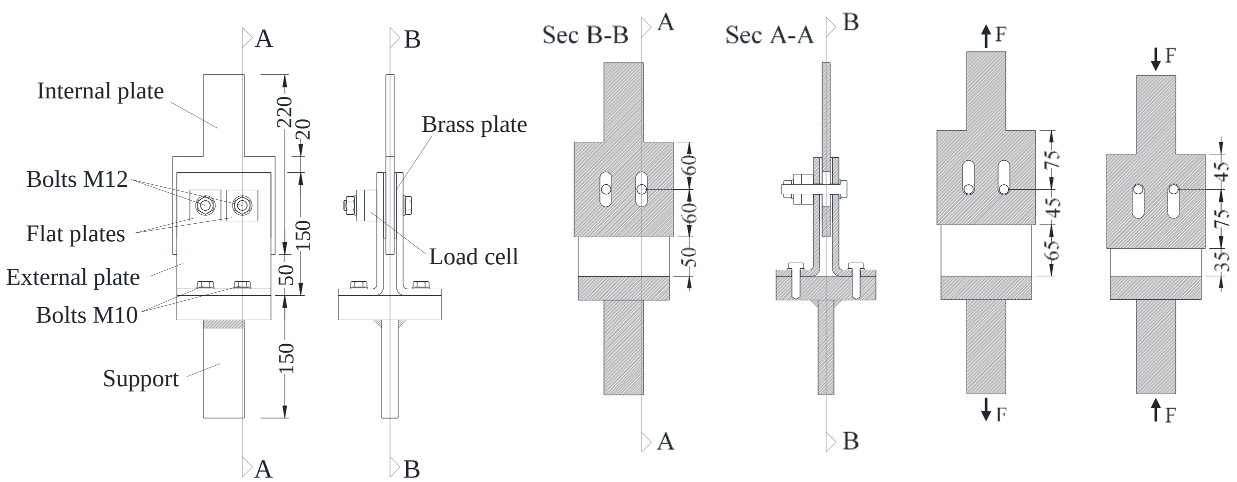


**Fig. 10.** Characterization test for the friction devices (FDs). Friction coefficient. Dimensions under the maximum and minimum displacement configuration (dimensions in mm)

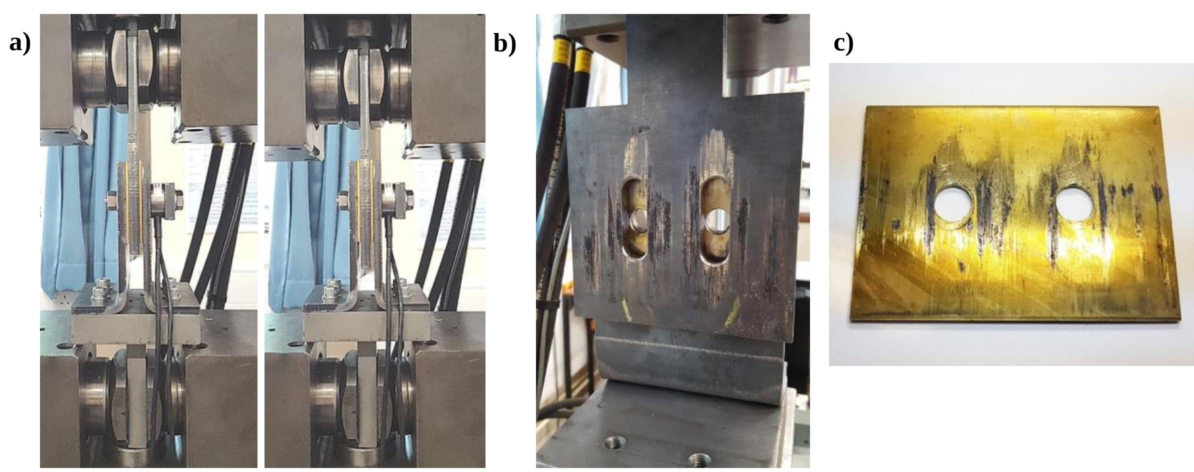


**Fig. 11.** Characterization test for the friction devices (FDs). Friction coefficient. (a) Front view with maximum and minimum displacements of the friction device (FD); (b) internal plate with slotted holes and (c) brass plate with circular holes after the test

The friction coefficient was determined by

$$\mu_{\mathrm{FD}} = \frac{F_{\mathrm{FD}}}{m \cdot n \cdot N_{\mathrm{b}}} \tag{14}$$

where $m$ = 2 is the number of surfaces in contact, $n$ = 2 is the number of bolts, $N_{\mathrm{b}}$ is the bolt pre-loading force while $F_{\mathrm{FD}}$ is the sliding force. The results of Fig. 12 and Fig. 13 refer to the test with the bolts' pre-loading force equal to 15 kN. Fig. 12(a) shows the displacement and force history, respectively, for the whole duration of the test, while Fig. 12(b) shows the results for the cycle from 50 to 56 seconds. Fig. 13(a) shows the force-displacement response that, considering the average normal force acting on the friction interface during the whole load history, which is equal to 33.47 kN, allowed to derive Fig. 13(b) which shows the friction coefficient according to Eq. (14).

Fig. 13(a) shows the force-displacement behavior exhibiting a slight kinematic hardening similarly to what was observed by Latour *et al* (2015). This is due to the changes in the contact surfaces, which were initially smooth. During sliding motion, the number of asperities increased due to the high contact pressures and to the wearing of the brass, causing an increase in interlocking friction components in the final surface, as shown in Fig. 11(b) and (c). Fig. 13(a) shows an increase of the friction coefficient that, after a few cycles, become stable with an increased sliding force of the order of 10 % with respect to the force corresponding to the first sliding. Consistent results were obtained for the other pre-loading forces and the average value of the friction coefficient, $\mu_{\mathrm{FD}}$, was equal to 0.25. It is important to highlight that for the pre-loading force of 25 kN, debonding of the external plate with the interface plate was observed. For this reason, a limited value of the bolts pre-loading force was used in the full-test of the column base as described in Section 7.

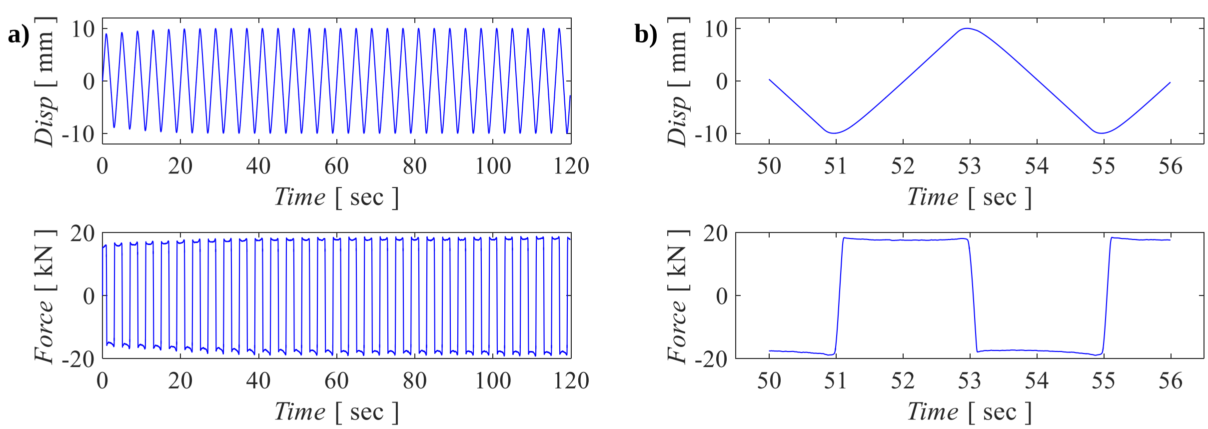


**Fig. 12.** Characterization test for the friction devices (FDs). Displacement and force history of the friction device (FD) test with pre-loading force in each bolt of 15 kN

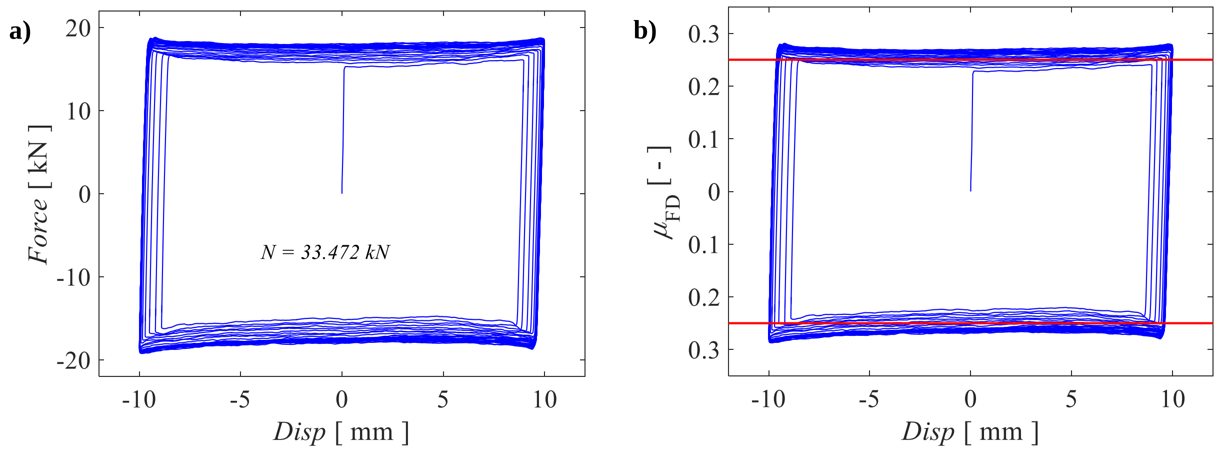


**Fig. 13.** Characterization test for the friction devices (FDs). Initial pre-loading force in each bolt of 15kN. (a) Force–displacement hysteretic curve and (b) normalized force for the definition of the friction coefficient $\mu_{FD}$

## 6. COUPON TESTS

The elements experiencing stresses beyond their yield stress (for rotations larger that the $\theta_T$) included the post-tensioned strands and the FDs. Certificates for the strands' stress-strain behavior were available from the supplier. For the characterization of the material properties of the plates of the FDs, coupon tests were performed using of the universal testing machine DARTEC 9500. Three coupon specimens for the FDs' plates were subjected to tensile tests according to the EN ISO 6892-1 (2009). Specimen strains were measured using an axial extensometer. Average values of the properties of the steel for each component are listed in Table 5.

**Table 5**. Steel Properties

| Test | Yield Stress [ MPa ] | Yield Strain [ % ] | Young Modulus [ MPa ] | Tensile Strength [ MPa ] | Maximum Elongation [ % ] |
|---|---|---|---|---|---|
| 1 | 335 | 0.166 | 201807 | 467 | 31.5 |
| 2 | 327 | 0.165 | 198181 | 452 | 32.7 |
| 3 | 332 | 0.164 | 202439 | 457 | 30.2 |
| Average Values | 331.3 | 0.165 | 200809 | 458.6 | 31.47 |

## 7. EXPERIMENTAL TEST ON THE ROCKING COLUMN BASE

### *7.1 Test setup and instrumentation*

The proposed column base was tested by using the test setup shown in Fig. 14 and illustrated in the photos of Fig. 15. The test setup was designed based on the space available in the lab and on the strong floor connections that were placed as a square wire every 406.4 mm.

### 7.2 PT bars

Two external Dywidag PT bars with diameter of 15 mm ($A_{PT,ext}$ = 177 mm$^2$; diameter after thread of 17 mm) and yield and ultimate stresses equal to $f_{y,PT,ext}$ = 900 MPa and $f_{u,PT,ext}$ = 1100 MPa, were used to simulate the axial forces due to gravity loads. The parameters affecting the stiffness of the PT bars were the free length and the Young's modulus, which were equal to $L_{PT,ext}$ = 1826.9 mm and $E_{PT,ext}$ = 205000 MPa. The PT bars were connected at one end to the upper beam, which transfers the force to the column, and at the other end to two anchor supports connected to the strong floor. Hollow hydraulic jacks type B (HJB in Table 3, in Fig. 14 and Fig. 16(a)) were used to apply the post-tensioning force. The load cells type C (LCC 1 and 2 in Table 4, in Fig. 14 and Fig. 16(b)) were used to calibrate the initial force and to measure its variation during the tests. After post-tensioning through the hydraulic jacks, intermediate bolts, as shown in Fig. 16(a), were placed and tightened to the web of the upper beam to avoid loss of PT force as consequence of the loss of pressure in the hydraulic jacks. The design initial PT force for the external bars was equal to 96.3 kN. During the rocking, the uplift of the column base produced an increase of the tension force of the PT bars which was measured during the test.

In addition to the axial force imposed by the PT bars, the total force was increased by the weight of all the components of the specimen and of the test setup. The weight of the upper beam and the column were respectively equal to 175 kg and 180 kg, while the total weight was equal to 430 kg. This value does not account for half of the weight of the horizontal actuator and hinges that was equal to 130 kg.

### 7.3 Steel basement and post-tensioned strands

The column was placed on a steel basement, which included the anchor plates for the strands as shown in Fig. 14, Fig. 16(c) and (e). The strands were fixed to the anchor plate of the steel basement from one side, and post-tensioned through hollow hydraulic jacks type A (HJA in Table 3, in Fig. 14 and Fig. 16(g)), which were supported by the anchor plate of the column base on the other side. Similar to the external PT bars, the strands were fixed to the upper anchor plate by the intermediate anchor grips to avoid loss of PT force. This was made possible thanks to the supports shown in Fig. 14 and Fig. 16(g). The design PT force for the strands was equal to 21.3 kN. The anchor grips were composed by wedges coupled with open barrels as showed in Fig. 16(d). Four load cells type B (LCB in Table 4, in Fig. 14 and Fig. 16(e)) were located between the anchor grips and the anchor plates in the steel basement to calibrate the initial post-tensioning force in the strands and to measure force variations during the tests. The upper plate of the steel basement was provided with oversized holes so that the strands were free to move laterally during the column rocking.

In addition, the upper plate included threaded holes for the connection of the FDs and the shear key. Fig. 16(c) shows the shear key fixed to the steel basement.

### 7.4 *Friction devices*

Each external plate of the FDs was bolted to the steel basement with two M10 bolts. The FDs had the same configuration used in the characterization tests with the only exception that the internal plates had inclined slotted holes to accommodate the bolts travel path. The internal plates were welded to the column as shown in Fig. 16(h) and (i). Four load cells type A (LCA in Table 4, Fig. 14 and Fig. 16(h)) were used to measure the variation of the axial force in four of the eight bolts of the FDs.

According to the original design, the bolts' pre-loading force in the friction devices was equal to 21.74 KN. This required a tightening torque equal to $T_b$ = 45.47 Nm. However, to avoid the debonding of the brass plates, that was observed in the FDs' characterization tests, and which could jeopardize the full-scale tests, the bolts' pre-loading force was set to 10 kN by applying a tightening torque, $T_b$, of 20.92 Nm.

### 7.5 *Other components*

LVDTs 1 to 4, as shown in Fig. 14 and Fig. 16(g), were placed in the column base at different heights in order to measure the horizontal translations, rotations in the longitudinal direction, as well as, the horizontal translations in the transverse direction and torsions. Moreover, in order to evaluate the stresses and deformation of the circular hollow cylinder of the column base, two strain gauges at each side, were introduced in the position close to the pivot points of the rocking as shown in Fig. 16(h). Finally, the specimen was connected with the horizontal actuator, which was fixed to a steel strong frame as shown in Fig. 15. The actuator was connected at both the ends by hinges to avoid any transfer of moment to the column.

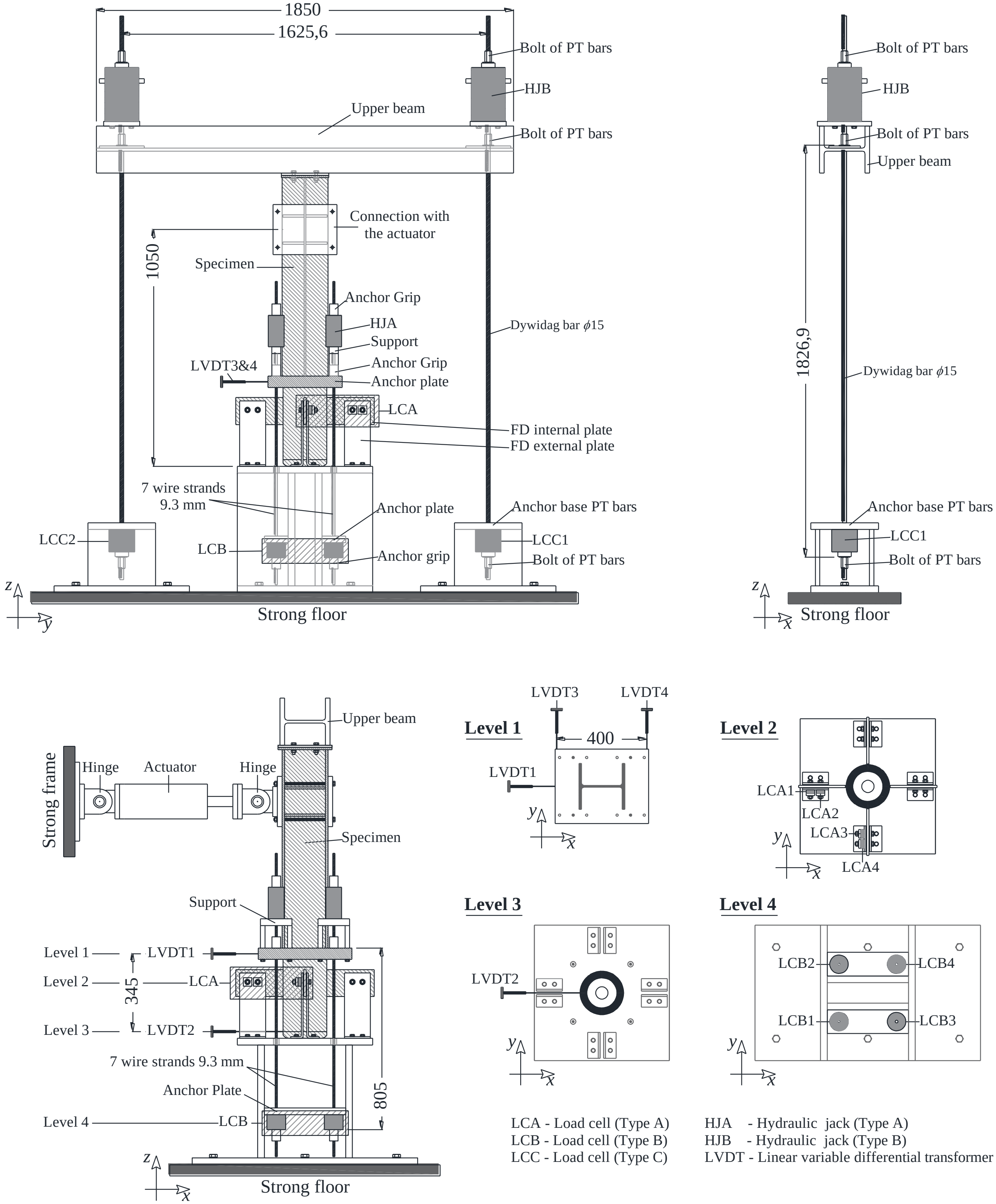


**Fig. 14.** Tests Setup and instrumentation (dimensions in mm)

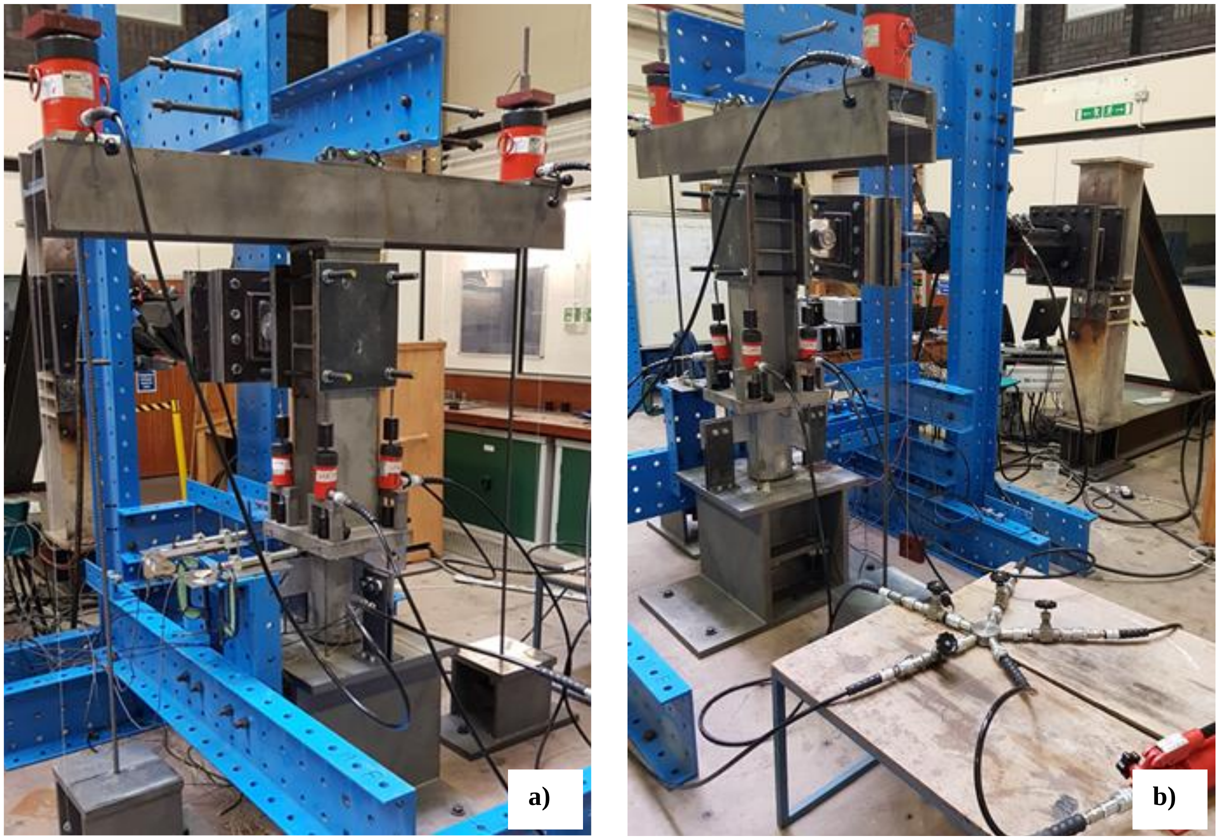


**Fig. 15.** Full-test setup

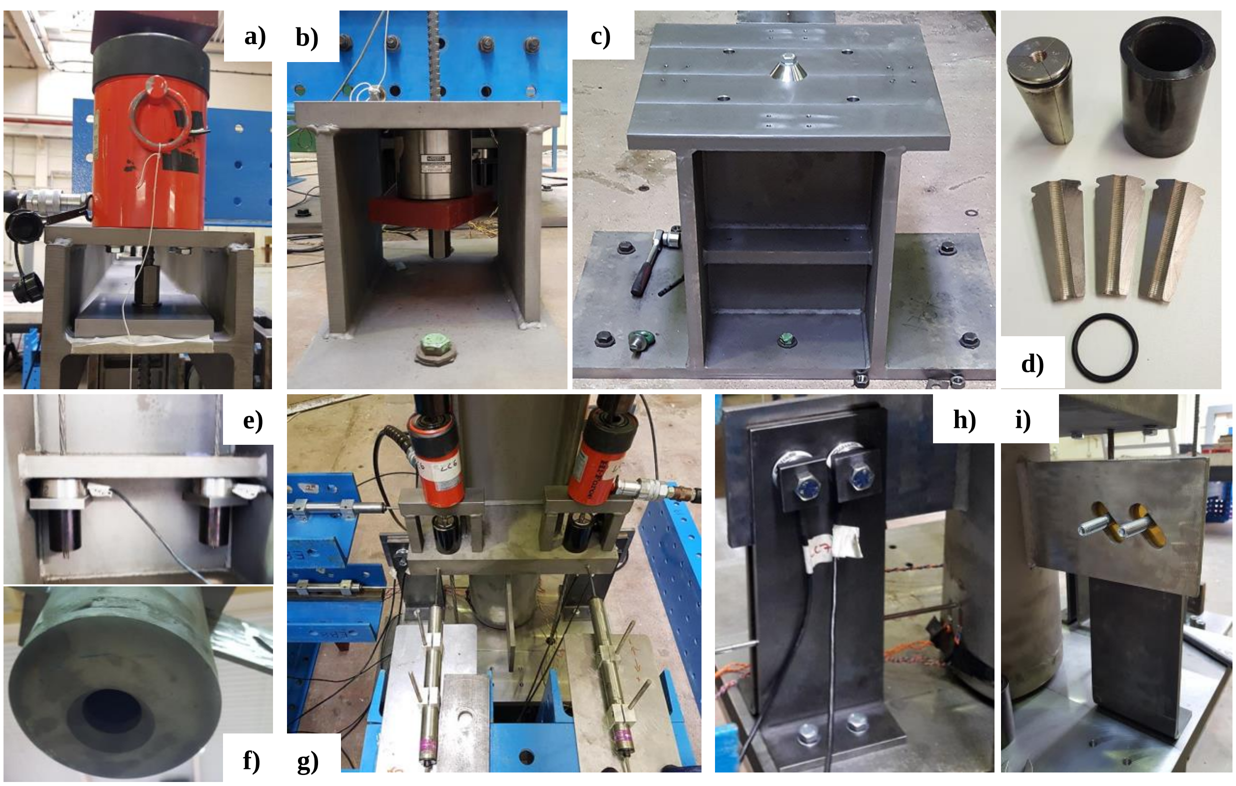


**Fig. 16.** Full-test setup components and instrumentation

## 8. EXPERIMENTAL RESULTS

Quasi static cyclic tests were performed for different configurations that included different components of the column base, *i.e.*, PT bars for the axial force only (test type A); PT bars and strands only (test type B); PT bars, strands, and FDs in the longitudinal direction only (test type C); and the complete column base (test type D), as indicated in Table 6. This allowed to experimentally decouple the moment contributions from each component. Preliminary tests were performed with different amplitudes without overcoming the elastic behavior of the strands and up to the target design rotation, $\theta_T$. The results of these cyclic tests are shown, for all the tests' configurations, in Fig. 17 and Fig. 18. Additionally, a final test with cyclic displacements of increasing amplitude was conducted showing the damage-free behavior of the column base up to the target design rotation, $\theta_T$ while for amplitudes higher than $\theta_T$, yielding of the strands occurred, and the failure of the FDs' plates due to bolts bearing was observed for very large rotations. The results are shown in Fig. 20 and Fig. 21.

**Table 6**. Tests configurations

| Test types | Components included |
|---|---|
| A | PT bars |
| B | PT bars and PT strands |
| C | PT bars, PT strands and longitudinal FDs |
| D | PT bars, PT strands, longitudinal and transverse FDs |

It is worth mentioning that, while the analytical formulation reported in Sections 2 and 3 considers only the rotation related to the gap opening, the column base rotation observed during the test, and reported in the following part of the paper, was measured based on the relative displacement of the LVDTs 1 and 2 divided by the distance between the two and hence accounts also for the deformability of the test setup. Moreover, it is important to point out the difficulties in applying the exact values of the initial forces in PT bars, strands, and bolts. However, these differences between the designed column base and the one actually tested, do not affect the final outcomes of the experimentation. The applied forces were measured in the experimental tests and FE models were successively adjusted to replicate the forces measured during the tests to evaluate their ability to represent the experimental results. Similarly, the test setup was included in the numerical model to account for its deformability. The numerical models were developed in ABAQUS (2013) and are discussed in Section 9.

*8.1 Preliminary tests*

Fig. 17 shows the experimental results for the cyclic test of column base type A for rotations up to about 0.045 rads. Fig. 17(a) shows the moment-rotation curve, while Fig. 17(b) shows the tension force variation in the PT bars. Similarly, Fig. 18 shows the experimental results for the cyclic test up to the target rotation ($\theta_T$ = 0.03 rads, 3 % drift) for the column base types B, C, and D. Fig. 18(a) shows the moment-rotation curves where it can be observed the elastic behavior of the column base type B and the influence of the FDs in dissipating energy. The small difference between the curves C and D shows the low influence of the transverse FDs as consequence of their small displacement and short lever arm with respect to the pivot point of rocking. However, their presence allows to dissipate the seismic energy when the column is subjected to loads in a different direction. The small residual displacement was related to the imperfections of the coupling of the column base plate with the steel basement, as will be discussed in Section 9. Fig. 18(b) shows the tension in the PT bars and as expected for these components, there is a superposition of the curves for column base types B, C, and D. The same applies for the strands' tension force and the strain gauges' measurements, as such, for simplicity, only the results of the column base type B are shown. Fig. 18(c) shows the tension force variation in the strands. Their initial PT force was equal to 29.65 kN with very small differences from strand to strand. Their behavior was elastic and, the tension force showed different stiffness for negative and positive values of the rotation due to the change of the pivot point when rocking which results in changes to the length of the lever arm. Fig. 18(d) shows the strain gauges measurements. Only strain gauges 1, 2, and 4 are shown since strain gauge 3 was damaged during the test. The results show the compression and decompression of the column edge while rocking, demonstrating the elastic behavior of the material.

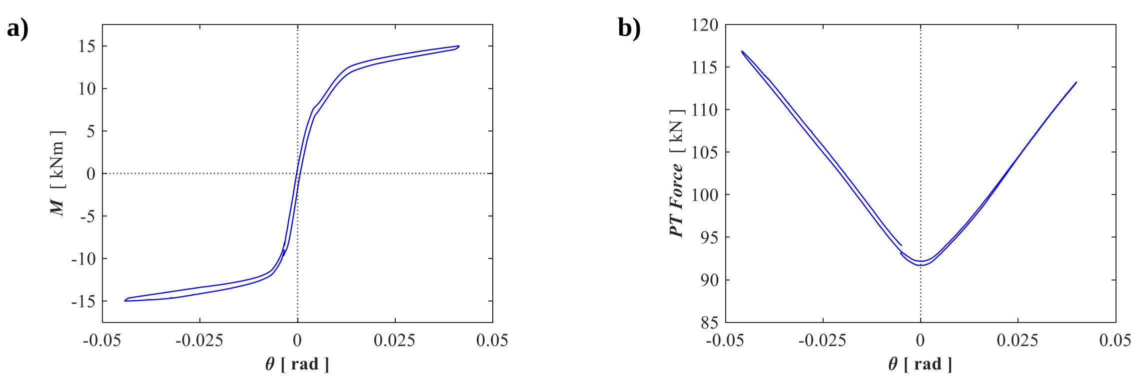


**Fig. 17.** Cyclic test of the column base type A. (a) Moment-rotation curve and (b) tension force in the PT bars

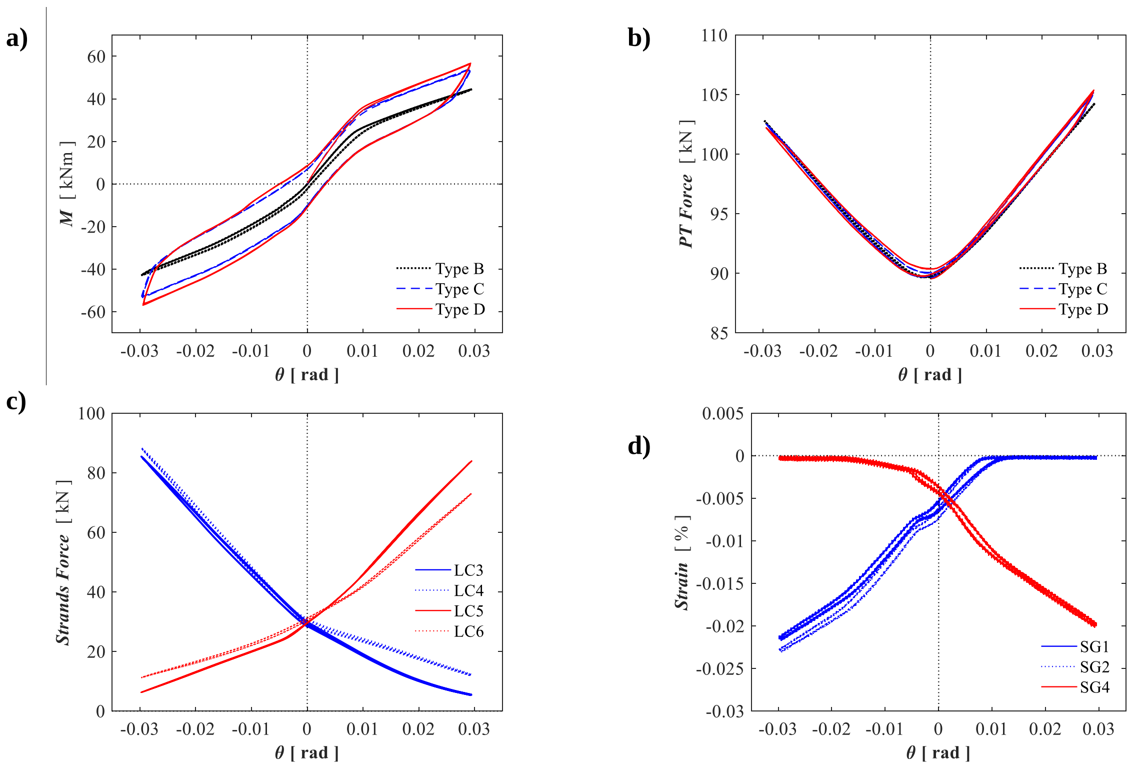


**Fig. 18.** Cyclic test of the column base types B, C and D up to the target rotation. (a) Moment-rotation curve; (b) PT bars tension force; (c) strands' tension force for the column base type B and (d) strain gauges' records the column base type B

### *8.2 Final tests*

The final test was conducted on the complete column base (type D) with increasing amplitudes up to the first component's failure by using a loading protocol that complies with the test requirements of AISC 341-16 (2005) for 'link-to-column moment connections'. The load protocol consisted of cyclic lateral displacements with increasing amplitude imposed in a quasi-static fashion as reported in Table 7. The protocol included three initial sets of six cycles at 8.25, 11, and 16.5 mm displacements, four subsequent cycles at 22 mm, and five sets of two cycles at 33, 44, 66, 88 and 100 mm. The specimen was also monotonically pushed to a displacement equal to 150 mm to identify the failure mode. Fig. 19 shows two displacements configurations considering the column at the onset of rocking on the right and left edges respectively for rotations of 0.095 and 0.143 rads (9.5 % and 14.3 % drift).

Fig. 20(a) shows the moment-rotation curves for cycle types from 1 to 5 with displacements amplitudes up to 33 mm (0.0314 rads, 3.14 % drift) while Fig. 20(b) shows the moment-rotation curves for the whole test. Fig. 21 shows the results for the moment-rotation curves, tension in the PT bars, tension in the strands, measurements from the strain gauges, and tension force in the bolts independently for the cycle types from 1 to 5, 6 and 7 and from 8 to 10. In this figure, together with the cycles in the displacement interval, the dotted black line shows also one cycle before and after, providing a better representation of the results' variation.

The results shown in Fig. 20(a) are similar to what is observed in the preliminary tests and show the elastic and damage-free behavior of the components up to the target rotation. Additional information provided by this final test are related to the behavior of the column base for rotations beyond the target one, as shown in Fig. 20(b) and more in detail in Fig. 21.

**Table 7**. Load protocol

| Cycle types | Number of cycles | Amplitude [ mm ] | Rotation [ rad ] | Drift [ % ] |
|---|---|---|---|---|
| 1 | 6 | 8.25 | 0.0078 | 0.78 |
| 2 | 6 | 11 | 0.0105 | 1.05 |
| 3 | 6 | 16.5 | 0.0157 | 1.57 |
| 4 | 4 | 22 | 0.0210 | 2.10 |
| 5 | 2 | 33 | 0.0314 | 3.14 |
| 6 | 2 | 44 | 0.0419 | 4.19 |
| 7 | 2 | 66 | 0.0629 | 6.29 |
| 8 | 2 | 88 | 0.0838 | 8.38 |
| 9 | 2 | 100 | 0.0952 | 9.52 |
| 10 | Monotonic up to 150 mm | | 0.1430 | 14.3 |

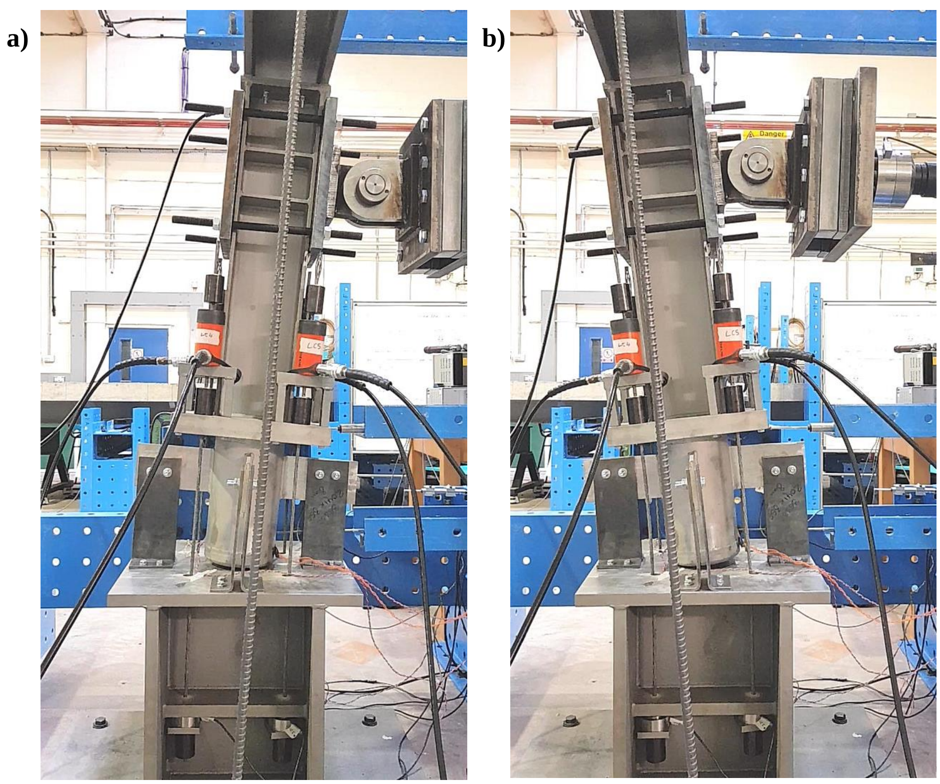


**Fig. 19.** Cyclic test for column type D. (a) Column rocking on the right edge with 0.095 rads (9.5 % drift) and (b) column rocking on the left edge with 0.143 rads (14.3 % drift)

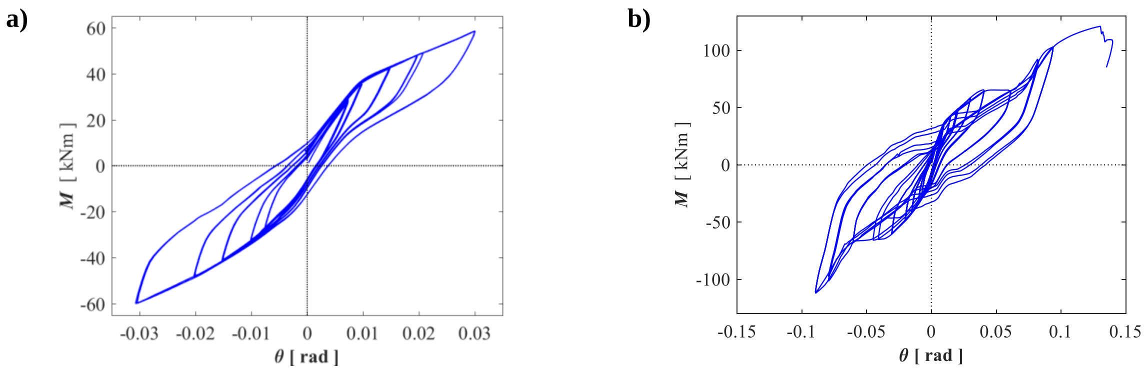


**Fig. 20.** Moment-rotation curve of the cyclic test for column type D for (a) cycle types from 1 to 5 with displacements amplitudes up to 33 mm (0.0314 rads, 3.14 % drift); (b) cycle for the whole test

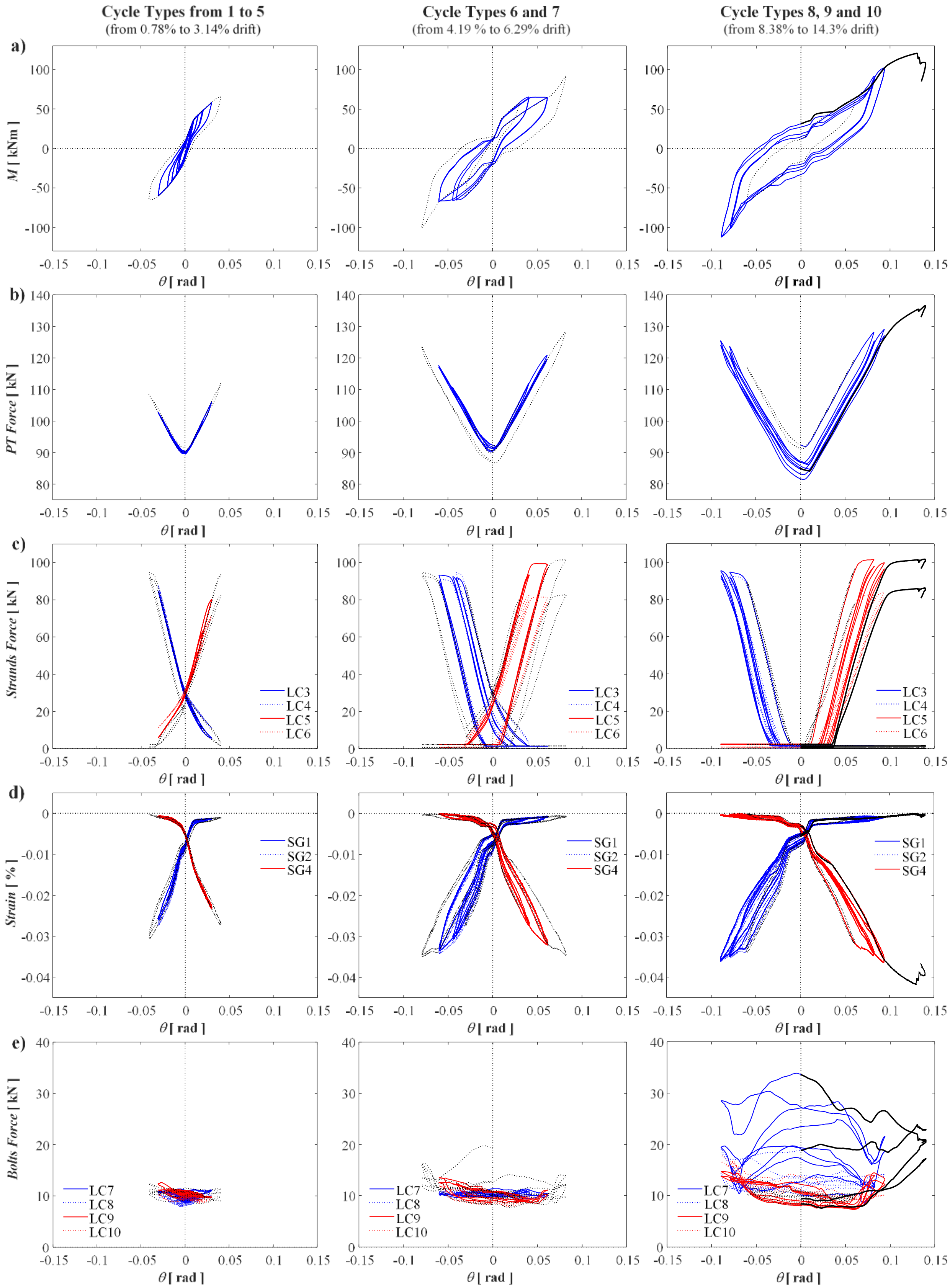


**Fig. 21.** Cyclic test for column type D. (a) Moment-rotation curve; (b) PT bars' tension force; (c) strands' tension force; (d) strain gauges' records and (e) bolts' tension force

For cycle types 1 to 5 of Fig. 21, the results were similar as that shown in Fig. 18 and were previously described.

For cycle type 6, and 7, Fig. 21(c) shows the strands' yielding which resulted in an increase of deformation with a nearly constant force. It is interesting to observe that the point when the first strands yielded, and the first loss of post-tensioning force correspond to a rotation of about 0.03 rads, as expected from the design. As a consequence of the yielding and of the residual elongation of the strands, their force corresponding to a zero rotation is equal to zero (*i.e.*, loss of post-tensioning force) at the end of cycle type 7. This affected the moment-rotation curve, shown in Fig. 21(a), where the post-elastic behavior exhibited low strain-hardening and reduction of the initial stiffness of the column base. Fig. 21(d) shows small post-elastic behavior of the column base's hollow section, as described by the strain gauges records. For these amplitudes there is no bearing of the FDs' bolts, as expected, based on the dimensions of the slotted holes and there was a nearly constant bolt tension force as shown in Fig. 21(e).

For cycle types 8, 9, and 10, Fig. 21(a) shows a significant increase of the stiffness in the moment-rotation curve. This is related to the bolts bearing, which was expected considering that the slotted holes of the FD were designed for rotations up to 0.06 rads and as a consequence, Fig. 21(e) shows a significant increase of the longitudinal bolts' tension force. Moreover, the increase of rotation amplitudes leaded to further yielding of the strands and of the hollow section of the column base, as shown in Fig. 21(c) and (d). Additionally, Fig. 21(b) shows the behavior of the PT bars that, in this case, experienced small plastic deformations and loss of PT force. However, this small reduction of the axial force in the column do not significantly affect the final results of the experimental test.

The black solid lines, shown in the figures for cycle types 8, 9, and 10, show the final monotonic increase of displacement leading to failure. Failure of one of the base bolts of the longitudinal FD in tension was observed for a rotation of about 0.014 rads (14 % drift) as shown in Fig. 22(a).

Observation of the specimen after the final test allowed to identify the damaged components, *i.e.*, the strands and the FDs undergoing plastic deformations. Fig. 22(a) and (b) show respectively the failure in the bolt and the residual deformation in the base plates of the FD, while Fig. 22(c) shows the residual deformations in one strand. For amplitudes within the target design rotation ($\theta_T$ = 0.03 rads), the column base showed damage-free behavior, while for very high rotations, even those significantly beyond the rotations of interest in earthquake engineering ($\theta \sim 0.14$), the column base showed the ability to isolate damage in few easily replaceable components, demonstrating its high potential to be used in highly earthquake-resilient steel structures.

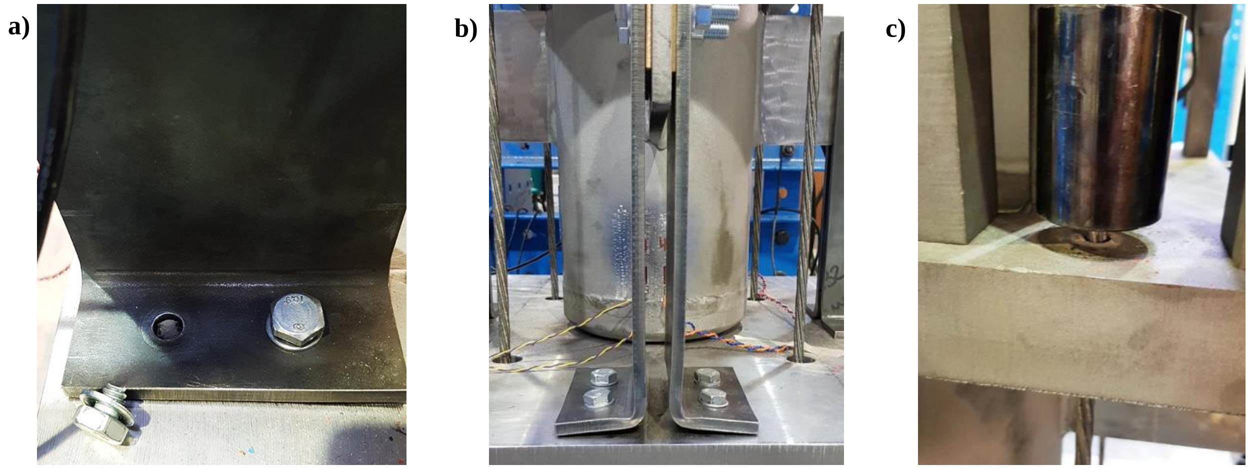


**Fig. 22.** Damage observed after the final cyclic test for column type D. (a) Failure of the FD's bolt; (b) residual deformations in the FDs' plates and (c) residual deformations in the strands

## 9. NUMERICAL ANALYSIS

A detailed 3D numerical model of the column base was developed in ABAQUS (2013). All the components were modeled using the eight-node linear brick element, which relies on reduced integration and hourglass control, while meshing was carried out using the structured and swift mesh techniques. The multi-point constraint was used to simulate the weldings (*i.e.,* monolithic connection), while the contacts were modeled by the surface-to-surface interaction property. This was implemented by the no penetration contact condition for the behavior in the normal direction with the interface plane and by the penalty method for the tangential response. In the FDs the friction coefficient was defined based on the results of the characterization tests. The initial post-tensioning forces in bolts was modeled such as it remains constant throughout the analysis, differently, for the PT bars the post-tensioning force can varies according to the elongation or shortening during rocking. The nonlinear behavior of the materials was modeled by the von Mises yield criterion coupled with isotropic hardening by using the material properties obtained by the coupon tests. The static analysis procedure was used to solve the nonlinear equilibrium equations while the standard Newton solution technique was used for the application of the loads. Additional modeling details are provided in Freddi *et al* (2017).

The FE model in ABAQUS (2013) included the column base as well as the test setup components, as shown in Fig. 23 in order to account for their deformability. Fig. 24 shows the comparison of the experimental and numerical results. It is worth noticing that, even before calibration, the ABAQUS model exhibited a quite accurate representation of the column base's behavior. Fig. 24(a) and (b) shows the moment-rotation curves of column base types B and D. Variation of the force in the PT bars and in the strands are shown, respectively in Fig. 24(c) and (d) for column base type B. Similar results were obtained for the other types, C and D.

The main difference between the numerical and experimental results is related to the reduced initial stiffness measured in the experimental tests and observed through comparison of the moment-rotation curves shown in Fig. 24(a) and (b). This is often the case when comparing experimental and numerical results, and in the present case, this difference is mainly related to the imperfections in the coupling between the column base plate with the steel basement.

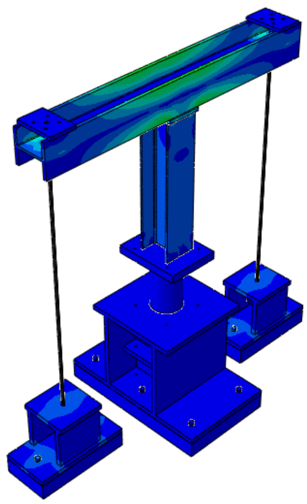

**Fig. 23.** Finite Element Model of the experimental test in ABAQUS (2013)

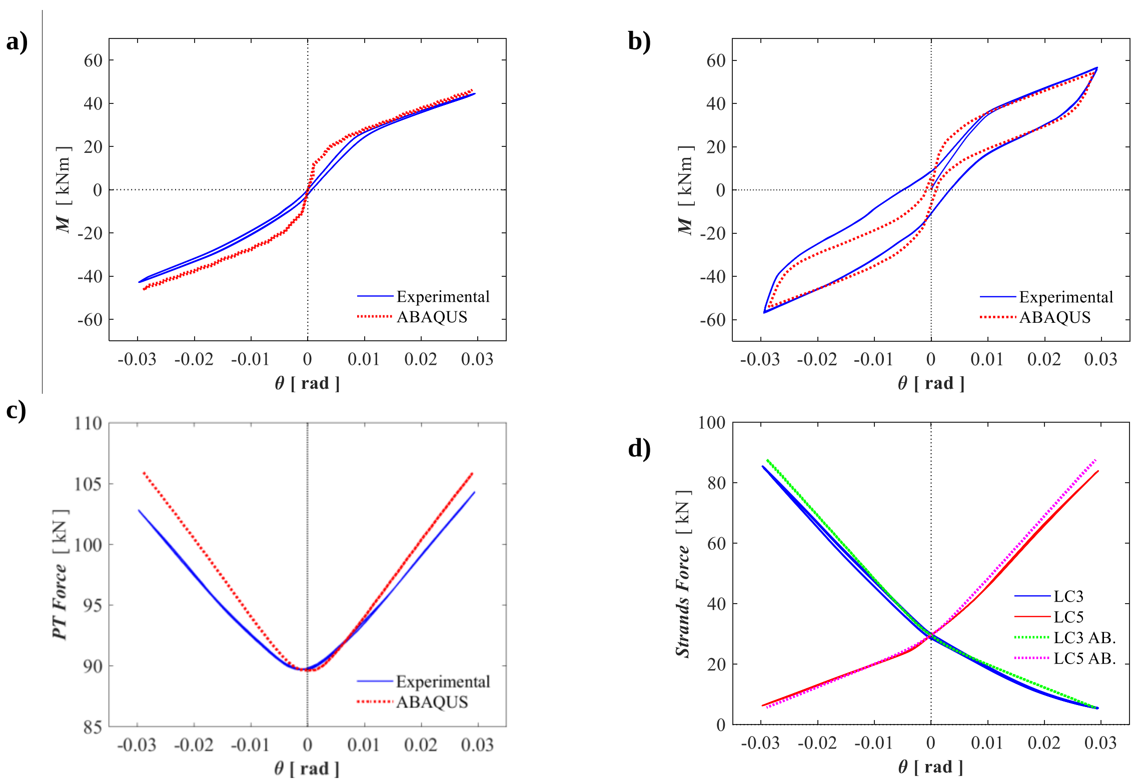


**Fig. 24.** Comparison between the experimental and numerical results in ABAQUS for the cyclic test up to the target rotation for: (a) Moment-rotation curve of column base type B; (b) Moment-rotation curve of column base type D. (c); PT bars tension force for the column base type B and (d) strands' tension force for the column base type B

Imperfections have been assessed according to the EN 1090-2 (2008) and included in the numerical ABAQUS models for the column base type D. The considered imperfection consisted of geometrical deviation in the plate with rounded edges and affected the contact conditions.

Without the imperfection, the central part of the steel plate with rounded edges is flat and in full contact with the steel basement. If the model account for these imperfections, the contact surface is limited before rocking. The local imperfection has been modeled as a symmetrical geometrical deviation as shown in Fig. 25(a).

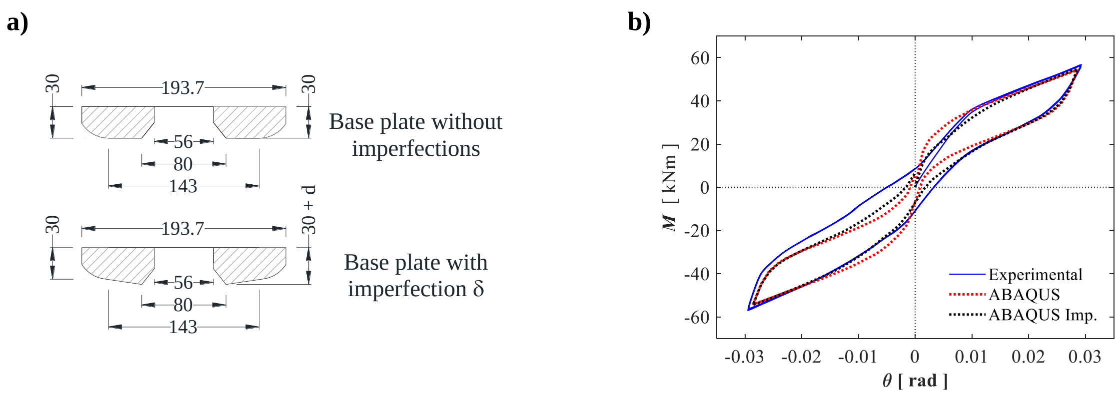


**Fig. 25.** (a) Imperfections modelling: geometrical deviation in the plate with rounded edges; (b) Comparison between the experimental and numerical moment-rotation curves for the cyclic test up to the target rotation for the of column base type D. ABAQUS models with and without imperfections

Several geometrical deviation amplitudes δ were investigated, *i.e.*, 0.3 mm, 0.7 mm, 1.0 mm and 1.4 mm and compared with the 'perfect' model ($\delta$ = 0.0 mm). Fig. 25(b) shows, for the column type D, the comparison of the experimental results with the numerical results for the 'perfect' model and the model with a geometrical deviation with amplitude $\delta$ = 0.3 mm. The comparison shows the impact that the imperfection can have on the initial stiffness without though affecting the moment-rotation response for rotations after the decompression.

Fig. 26 shows the comparison of the contact stresses for different rotation values of the column base with and without imperfections. It can be observed that the evolution of contact stresses is significantly different at the beginning of rocking, *i.e.*, the contact surface 'moves quickly' to the steel plate edge in the 'perfect' model while the transition requires a larger rotation in the case with imperfections. This influences the initial stiffness of the system. As a consequence of the imperfections, the distribution of stresses in the initial phase is significantly different, *i.e.*, at the end of post-tensioning of the PT bars and strands, the contact stresses are very localized in the imperfect models at the position where the imperfection amplitude is largest, while in the 'perfect' case, the contact stresses are distributed nearly uniformly over the whole surface of the steel plate.

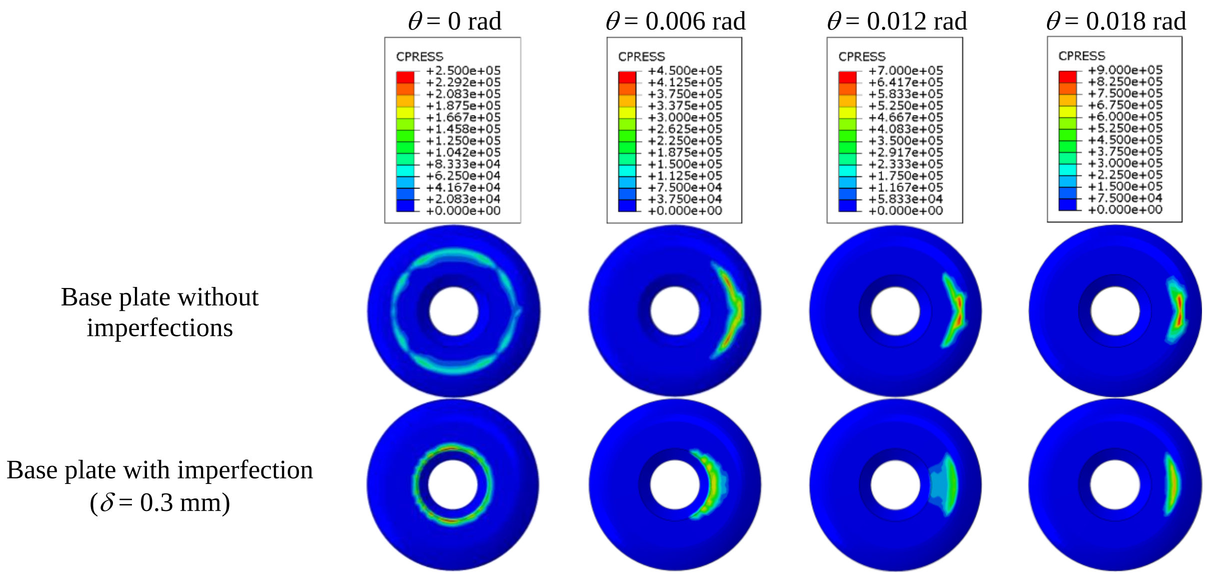


**Fig. 26.** Contact stresses for different rotation values of column base with and without imperfections

The results show that the initial stiffness of the rocking system is significantly affected by this type of initial imperfection. Careful manufacturing process would allow a reduction of initial imperfection improving the confidence on the column base behavior. However, the results show that, even without considering the imperfections, the analytical formulation and the numerical model allow to capture the behavior of the column base after the decompression moment.

## 10. CONCLUSIONS

An earthquake-resilient rocking steel column base previously proposed and numerically investigated by the authors is experimentally tested. The proposed column base can be used to reduce residual deformations and damage in 'innovative' MRFs where the variations in the axial force associated with seismic overturning moment is limited. The column base uses post-tensioned (PT) high strength steel bars to control rocking behavior and friction devices (FDs) to dissipate seismic energy. A column base extracted from a prototype steel building was designed using a step-by-step design procedure, previously proposed by the authors, that aims to achieve damage-free and self-centering behavior for a predefined target rotation. Component tests for the characterization of the FDs were conducted to assess the relationship between the torque applied to high-strength bolts and the resistance (force corresponding to initiation of sliding) of the FDs. The experimental tests were conducted on a 3/5 scaled column base under monotonic and cyclic quasi-static lateral loading protocols while simulating an about constant axial force. The experimental results showed good agreement with the expected behavior from analytical equations, which validated the design procedure.

Moreover, they demonstrated the damage-free behavior up to the target design rotation and the ability to limit the damage only to few easily replaceable components under large rotations. This demonstrates the high potential of the innovative column base to be used in earthquake-resilient steel structures. The experimental results were also used to calibrate refined 3D numerical models in ABAQUS that allowed to investigate the influence of the imperfections. Amongst others, future research should focus on performing experimental dynamic tests to fully assess the seismic performance of the proposed column base allowing the evaluation of the effect of the energy radiated during impact. Moreover, additional research is required to reduce the uncertainty of the FDs response as consequence of the variability of the bolt preload and the friction coefficient with time.

## DATA AVAILABILITY

All data, models, or code generated or used during the study are available from the corresponding author by request.

## ACKNOWLEDGEMENTS

This research is supported by Marie Sklodowska-Curie Action Fellowships within the H2020 European Programme. Any opinions, findings, and conclusions or recommendations expressed in this paper are those of the authors and do not necessarily reflect the views of the European Commission. The Authors also gratefully acknowledge the support of Prof. J. Toby Mottram and the work of the technicians of the Structural Testing Laboratory of the University of Warwick: Taylor Arnett and Neil Gillespie.

## REFERENCES

ABAQUS/Standard and ABAQUS/Explicit – Version 6.13.1. ABAQUS Theory Manual, Dassault Systems, 2013.

Akcelyan, S., Lignos, D.G., Hikino, T., Nakashima, M. (2016). "Evaluation of Simplified and State-of-the-Art Analysis Procedures for Steel Frame Buildings Equipped with Supplemental Damping Devices Based on E-Defense Full-Scale Shake Table Tests." *J. Struct. Eng.*; **142**(6), 04016024.

ANSI/AISC 341-05. (2005) "Seismic Provisions for Structural Steel Buildings." *American Institute of Steel Construction*, Chicago, Illinois.

Blomgren H-E., Pei, S., Jin, Z., Powers, J., Dolan, J.D., van de Lindt, J.W., Barbosa, A.R., Huang, D. (2019). "Full-Scale Shake Table Testing of Cross-Laminated Timber Rocking Shear Walls with Replaceable Components." *J. Struct. Eng.*; **145**(10), 04019115.

Borzouie, J., MacRae, G.A., Chase, J.G., Rodgers, G.W., Clifton, G.C. (2015). "Experimental studies on cyclic performance of column base strong axis – aligned asymmetric friction connections." *J. Struct. Eng.*; **142**(1), 04015078, 1–10.

BSI Standards Publication. (2012). "High tensile steel wire and strand for the prestressing of concrete - Specification". *BS 5896:2012, The British Standards Institution*, London, UK.

Chi, H., Liu, J. (2012). "Seismic behavior of post-tensioned column base for steel self-centering moment resisting frame." *J. Constr. Steel Res.*, **78**, 117–130.

Chou, C-C., Chen, J.H. (2011). "Analytical model validation and influence of column bases for seismic responses of steel post-tensioned self-centering MRF systems." *Eng. Struct.*, **33**(9), 2628–2643.

Coelho, A., Bijlaard, F., Gresnigt, N., da Silva, L.S. (2004). "Experimental assessment of the behavior of bolted T-stub connections made up of welded plates." *J. Constr. Steel Res.*; **60**(2), 269–311.

CSI SAP2000. (2011). "Linear and Nonlinear Static and Dynamic Analysis and Design of Three-Dimensional Structures: Basic Analysis Reference Manual". *Computers and Structures*, Inc. Berkeley, California.

Dimopoulos, A.I., Tzimas, A.S., Karavasilis, T.L., Vamvatsikos. D. (2016). "Probabilistic economic seismic loss estimation in steel buildings using post-tensioned moment-resisting frames and viscous dampers." *Earthquake Eng. Struct. Dyn.*; **45**(11), 1725-1741.

Dimopoulos, C., Freddi, F., Karavasilis, T. (2019). "Progressive collapse resistance of steel self-centering MRFs including the effects of the composite floor." *Engineering Structures*. https://doi.org/10.1016/j.engstruct.2019.109923

EN 1090-2. (2008) "Execution of steel structures and aluminum structures - Part 2: Technical requirements for steel structures." *European Committee for Standardization*, Brussels, Belgium.

EN 1991-1-1. (2001). "Eurocode 1: Actions on structures – Part 1-1: General actions – Densities, self-weight, imposed loads for buildings." *European Committee for Standardization*, Brussels, Belgium.

EN 1993-1-1. (2005). "Eurocode 3: Design of steel structures – Part 1-1: General rules and rules for buildings." *European Committee for Standardization*, Brussels, Belgium.

EN 1993-1-8. (2005). "Eurocode 3: Design of steel structures – Part 1-8: Design of Joints." *European Committee for Standardization*, Brussels, Belgium.

EN 1998-1-1. (2005). "Eurocode 8: Design of structures for earthquake resistance – Part 1: General rules, seismic action and rules for buildings." *European Committee for Standardization*, Brussels, Belgium.

EN ISO 6892-1. (2009) “Metallic materials - Tensile testing - Part 1: Method of test at room temperature.” *European Committee for Standardization*, Brussels, Belgium.

Federal Emergency Management Agency (FEMA). (2000). “Recommended seismic design criteria for new steel moment-frame buildings.” *FEMA 350, SAC Joint Venture*, Washington, DC.

Freddi, F., Tubaldi, E., Ragni, L., Dall’Asta, A. (2013). “Probabilistic performance assessment of low-ductility reinforced concrete frame retrofitted with dissipative braces.” *Earthquake Eng. Struct. Dyn.*; **42**(7), 993–1011.

Freddi, F., Dimopoulos, C.A., Karavasilis, T.L. (2017). “Rocking damage-free steel column base with friction devices: design procedure and numerical evaluation.” *Earthquake Eng. Struct. Dyn.*; **46**(14): 2281-2300. DOI: 10.1002/eqe.2904.

Garlock, M., Sause, R., Ricles, J.M. (2007). “Behavior and design of posttensioned steel frame systems.” *J. Struct. Eng.*; **133**(3), 389–399.

Gioiella, L., Tubaldi, E., Gara, F., Dezi, L., Dall'Asta A. (2018). “Modal properties and seismic behaviour of buildings equipped with external dissipative pinned rocking braced frames.” *Eng. Struct.*; **172**, 807–819.

Grauvilardell, J.E., Lee, D., Hajjar, J.F., Dexter, R.J. (2006). “Synthesis of design, testing and analysis research on steel column base plate connections in high-seismic zones.” *Report ST-04-02*, Dept. of Civil Engineering, Univ. of Minnesota, USA.

Grigorian, C.E., Yang, T.S., Popov, E.P. (1993). “Slotted bolted connection energy dissipators.” *Earthq. Spectra*: **9**(3): 491–504.

Haremza, C., Santiago, A., da Silva, L.S. (2013). “Experimental behavior of heated composite steel–concrete joints subject to variable bending moments and axial forces.” *Eng. Struct.*; **51**, 150–161.

Ikenaga, M., Nagae, T., Nakashima, M., Suita, K. (2006). “Development of column bases having self-centering and damping capability.” *5th Int. Conf. on Behaviour of Steel Structures in Seismic Areas*, Yokohama, Japan.

Kamperidis, V.C., Karavasilis, T.L., Vasdravellis, G. (2018). “Self-centering steel column base with metallic energy dissipation devices.” *J. of Constr. Steel Res.*; **149**, 14–30.

Kanvinde, A.M., Grilli, D.A., Zareian, F. (2012). “Rotational stiffness of exposed column base connections: experiments and analytical models.” *J. Struct. Eng.*; **138**(5), 549–560.

Kelly, J.M., Tsztoo, D.F. (1977). “Earthquake simulation testing of a stepping frame with energy-absorbing devices. *NZ Soc. Earthquake Eng. Bull.*; **10**(4): 196-207.

Kim, H.J., Christopoulos, C. (2008). “Seismic design procedure and seismic response of post-tensioned self-centering steel frames." *Earthquake Eng. Struct. Dyn.*, **38**(3), 355–376.

Latour, M., Rizzano, G. (2013). "Full strength design of column base connections accounting for random material variability." *Eng. Struct.*; **48**, 458–471.

Latour, M., Rizzano, G. (2013). "A theoretical model for predicting the rotational capacity of steel base joints." *Eng. Struct.*; **91,** 89–99.

Latour, M., Piluso, V., Rizzano, G. (2015). "Free from damage beam-to-column joints: Testing and design of DST connections with friction pads." *Eng. Struct.*; **85**, 219–233.

Latour, M., Rizzano, G., Santiago, A., da Silva, L.S. (2019). "Experimental response of a low-yielding, re-centering, rocking base plate joint with friction dampers." *Soil Dyn. Earthq. Eng.*; **116**: 580-592.

Mackinven, H., MacRae, G.A., Pampanin, S., Clifton, G.C., Butterworth, J. (2007). "Generation four steel moment frame joints." *8th Pacific Conf. on Earthq. Eng.*, Singapore.

MacRae, G.A., Urmson, C.R., Walpole, W.R., Moss, P., Hyde, K., Clifton, C. (2009). "Axial shortening of steel columns in buildings subjected to earthquakes." *Bull. New Zeal. Soc. Earthq. Eng.*, **42**(4): 275–287.

McKenna, F., Fenves, G.L., Scott, M.H. (2006). "OpenSees: Open system for earthquake engineering simulation." *PEER Center*, Berkeley, CA.Wolski, M., Ricles, J., Sause, R. (2009). "Experimental Study of a Self-Centering Beam–Column Connection with Bottom Flange Friction Device." *J. Struct. Eng.*; **135**(5), 479–488.

Rodas, P.T., Zareian, F., Kanvinde, A. (2016). "Hysteretic model for exposed column-base connections." *J. Struct. Eng.*; **142**(12), 04016137, 1–14.

Symans, M.D., Charney, F.A., Whittaker, A.S., Constantinou, M.C., Kircher, C.A., Johnson, M.W., McNamara, R.J. (2008). "Energy dissipation systems for seismic applications: Current practice and recent developments." *J. Struct. Eng.*; **134**(1), 3–21.

Takamatsu, T., Tamai, H. (2005). "Non-slip-type restoring force characteristics of an exposed-type column base." *J. Constr. Steel Res*. **61**(7): 942–961.

Tzimas, A.S., Kamaris, G.S., Karavasilis, T.L., Galasso, C. (2016). "Collapse risk and residual drift performance of steel buildings using post-tensioned MRFs and viscous dampers in near-fault regions." *Bulletin Earthq. Eng.;* **14**(6), 1643-1662.

Vasdravellis, G., Karavasilis, T.L., Uy, B. (2013). "Large-scale experimental validation of steel posttensioned connections with web hourglass pins." *J. Struct. Eng.*; **139**(6), 1033–1042.

Wang, X.T., Xie, C.D., Lin, L.H., Li, J. (2019). "Seismic behavior of self-centering concrete-filled square steel tubular

(CFST) column base." *J. of Constr. Steel Res.*; 156: 75–85.

Yamanishi, T., Kasai, K., Takamatsu, T., Tamai, H. (2012). "Innovative column-base details capable of tuning rigidity and strength for low to medium-rise steel structures." *15th World Conf. on Earthq. Eng.*, Lisbon, Portugal.

Zareian, F., Kanvinde, A. (2013). "Effect of column-base flexibility on the seismic response and safety of steel moment-resisting frames." *Earthq. Spectra*; **29**(4), 1537–1559.